Am J Physiol Heart Circ Physiol 291: H2187–H2191, 2006.
First published June 9, 2006; doi:10.1152/ajpheart.00175.2006.

Effects of Ca^{2+} channel antagonists on nerve stimulation-induced and ischemia-induced myocardial interstitial acetylcholine release in cats

Toru Kawada,[1] Toji Yamazaki,[2] Tsuyoshi Akiyama,[2] Kazunori Uemura,[1] Atsunori Kamiya,[1] Toshiaki Shishido,[1] Hidezo Mori,[2] and Masaru Sugimachi[1]

[1]*Department of Cardiovascular Dynamics, Advanced Medical Engineering Center, National Cardiovascular Center Research Institute and* [2]*Department of Cardiac Physiology, National Cardiovascular Center Research Institute, Osaka, Japan*

Submitted 17 February 2006; accepted in final form 7 June 2006

Kawada, Toru, Toji Yamazaki, Tsuyoshi Akiyama, Kazunori Uemura, Atsunori Kamiya, Toshiaki Shishido, Hidezo Mori, and Masaru Sugimachi. Effects of Ca^{2+} channel antagonists on nerve stimulation-induced and ischemia-induced myocardial interstitial acetylcholine release in cats. *Am J Physiol Heart Circ Physiol* 291: H2187–H2191, 2006. First published June 9, 2006; doi:10.1152/ajpheart.00175.2006.—Although an axoplasmic Ca^{2+} increase is associated with an exocytotic acetylcholine (ACh) release from the parasympathetic postganglionic nerve endings, the role of voltage-dependent Ca^{2+} channels in ACh release in the mammalian cardiac parasympathetic nerve is not clearly understood. Using a cardiac microdialysis technique, we examined the effects of Ca^{2+} channel antagonists on vagal nerve stimulation- and ischemia-induced myocardial interstitial ACh releases in anesthetized cats. The vagal stimulation-induced ACh release [22.4 nM (SD 10.6), $n = 7$] was significantly attenuated by local administration of an N-type Ca^{2+} channel antagonist ω-conotoxin GVIA [11.7 nM (SD 5.8), $n = 7$, $P = 0.0054$], or a P/Q-type Ca^{2+} channel antagonist ω-conotoxin MVIIC [3.8 nM (SD 2.3), $n = 6$, $P = 0.0002$] but not by local administration of an L-type Ca^{2+} channel antagonist verapamil [23.5 nM (SD 6.0), $n = 5$, $P = 0.758$]. The ischemia-induced myocardial interstitial ACh release [15.0 nM (SD 8.3), $n = 8$] was not attenuated by local administration of the L-, N-, or P/Q-type Ca^{2+} channel antagonists, by inhibition of Na^+/Ca^{2+} exchange, or by blockade of inositol 1,4,5-trisphosphate [Ins(1,4,5)P_3] receptor but was significantly suppressed by local administration of gadolinium [2.8 nM (SD 2.6), $n = 6$, $P = 0.0283$]. In conclusion, stimulation-induced ACh release from the cardiac postganglionic nerves depends on the N- and P/Q-type Ca^{2+} channels (with a dominance of P/Q-type) but probably not on the L-type Ca^{2+} channels in cats. In contrast, ischemia-induced ACh release depends on nonselective cation channels or cation-selective stretch activated channels but not on L-, N-, or P/Q type Ca^{2+} channels, Na^+/Ca^{2+} exchange, or Ins(1,4,5)P_3 receptor-mediated pathway.

cardiac microdialysis; ω-conotoxin GVIA; ω-conotoxin MVIIC; KB-R7943; verapamil; vagal stimulation

ALTHOUGH N-TYPE Ca^{2+} CHANNELS play a dominant role in norepinephrine release from sympathetic nerve endings (8, 33, 34), the type(s) of Ca^{2+} channels controlling ACh release in the mammalian parasympathetic system is not fully understood and show diversity among reports. To name a few, in isolated parasympathetic submandibular ganglia from the rat, neurotransmission is mediated by Ca^{2+} channels that are resistant to the L-, N-, P/Q-, and R- type Ca^{2+} channel antagonists (29). When the negative inotropic response to field stimulation was examined in the isolated guinea pig atria, Hong and Chang (8) reported the importance of P/Q-type Ca^{2+} channels, whereas Serone et al. (28) reported the importance of N-type Ca^{2+} channels. Because field stimulation in the isolated preparations could induce responses different from those in the in vivo conditions, we aimed to examine the effects of Ca^{2+} channel antagonists on the vagal nerve stimulation-induced myocardial interstitial ACh release in the in vivo feline heart.

Aside from the important role of the normal physiological regulation of the heart, the vagal nerve can be a therapeutic target for certain cardiovascular diseases (2, 3, 13, 22, 27). In previous studies, we have shown that acute myocardial ischemia causes myocardial interstitial ACh release in the ischemic region independently of efferent vagal nerve activity (12, 14). The comparison of the effects of Ca^{2+} channel antagonists on the ACh releases induced by vagal nerve stimulation and by acute myocardial ischemia may deepen our understanding about the ischemia-induced myocardial interstitial ACh release.

A cardiac microdialysis technique offers detailed analyses of in vivo myocardial interstitial ACh release (1, 15). Because the local administration of pharmacological agents through a dialysis probe can modulate ACh release without significantly affecting systemic hemodynamics, a combination of cardiac microdialysis with local pharmacological interventions is useful for analyzing the mechanisms of ACh release in vivo. In the present study, we examined the effects of Ca^{2+} channel antagonists on nerve stimulation- and ischemia-induced ACh releases in anesthetized cats. The results indicate that stimulation-induced ACh release from the cardiac parasympathetic postganglionic nerves depends on the N- and P/Q-type Ca^{2+} channels but probably not on the L-type Ca^{2+} channels. In contrast, ischemia-induced myocardial interstitial ACh release is resistant to the inhibition of L-, N-, and P/Q-type Ca^{2+} channels. In addition, the ischemia-induced myocardial ACh release is resistant to the inhibition of Na^+/Ca^{2+} exchanger and the blockade of inositol 1,4,5-trisphosphate [Ins(1,4,5)P_3] receptor but is suppressed by gadolinium, suggesting that nonselective cation channels or cation-selective stretch-activated channels are involved.

MATERIALS AND METHODS

Common Preparation

Animal care was provided in accordance with the *Guiding Principles for the Care and Use of Animals in the Field of Physiological*

Address for reprint requests and other correspondence: T. Kawada, Dept. of Cardiovascular Dynamics, Advanced Medical Engineering Center, National Cardiovascular Center Research Institute, 5-7-1 Fujishirodai, Suita, Osaka 565-8565, Japan (e-mail: torukawa@res.ncvc.go.jp).

The costs of publication of this article were defrayed in part by the payment of page charges. The article must therefore be hereby marked "*advertisement*" in accordance with 18 U.S.C. Section 1734 solely to indicate this fact.

Sciences approved by the Physiological Society of Japan. All protocols were approved by the Animal Subjects Committee of the National Cardiovascular Center. Adult cats weighing from 2.2 to 4.2 kg were anesthetized via an intraperitoneal injection of pentobarbital sodium (30–35 mg/kg) and ventilated mechanically with room air mixed with oxygen. The depth of anesthesia was maintained with a continuous intravenous infusion of pentobarbital sodium (1–2 $mg \cdot kg^{-1} \cdot h^{-1}$) through a catheter inserted from the right femoral vein. Systemic arterial pressure was monitored from a catheter inserted from the right femoral artery. The vagi were sectioned bilaterally at the neck. The esophageal temperature of the animal, which was measured by a thermometer (CTM-303, TERUMO, Japan), was maintained at around 37°C using a heated pad and a lamp.

With the animal in the lateral position, the left fifth and sixth ribs were resected to expose the heart. A dialysis probe was implanted transversely, using a fine guiding needle, into the anterolateral free wall of the left ventricle perfused by the left anterior descending coronary artery (LAD). Heparin sodium (100 U/kg) was administered intravenously to prevent blood coagulation. At the end of the experiment, the experimental animals were killed with an overdose of pentobarbital sodium. Postmortem examination confirmed that the dialysis probe had been threaded in the middle layer of the left ventricular myocardium. The thickness of the left ventricular free wall was ~7–8 mm, and the semipermeable membrane of the dialysis probe was positioned ~3–4 mm from the epicardial surface.

Dialysis Technique

The materials and properties of the dialysis probe have been described previously (1). Briefly, we designed a transverse dialysis probe. A dialysis fiber of semipermeable membrane (13 mm length, 310 μm OD, 200 μm ID; PAN-1200, 50,000 molecular weight cutoff, Asahi Chemical, Japan) was glued at both ends to polyethylene tubes (25 cm length, 500 μm OD, 200 μm ID). The dialysis probe was perfused at a rate of 2 μl/min with Ringer solution containing a cholinesterase inhibitor eserine (physostigmine, 100 μM). Experimental protocols were started 2 h after the dialysis probe was implanted when the ACh concentration in the dialysate reached a steady state. The ACh concentration in the dialysate was measured by high-performance liquid chromatography with electrochemical detection (Eicom, Kyoto, Japan).

Local administration of a pharmacological agent was carried out through a dialysis probe. That is to say, we added the pharmacological agent to the perfusate and allowed 1 h for a settling time. The pharmacological agent should spread around the semipermeable membrane, thereby affecting the neurotransmitter release in the vicinity of the semipermeable membrane. Because the distribution across the semipermeable membrane is required, based on previous results (33, 34), we used the pharmacological agent at the concentration 10–100 times higher than that required for complete channel blockade in experimental settings in vitro.

Specific Preparation and Protocols

Protocol 1. Bipolar platinum electrodes were attached bilaterally to the cardiac ends of the sectioned vagi at the neck. The nerves and electrodes were covered with warmed mineral oil for insulation. The vagal nerves were stimulated for 15 min (20 Hz, 1 ms, 10 V). We measured the stimulation-induced ACh release in the absence of Ca^{2+} channel blockade (control, $n = 7$) and examined the effects of an L-type Ca^{2+} channel antagonist verapamil (100 μM, $n = 5$), an N-type Ca^{2+} channel antagonist ω-conotoxin GVIA (10 μM, $n = 7$), a P/Q-type Ca^{2+} channel antagonist ω-conotoxin MVIIC (10 μM, $n = 6$), and combined administration of ω-conotoxin GVIA and ω-conotoxin MVIIC (10 μM each, $n = 6$).

Protocol 2. Because a preliminary result from *protocol 1* suggested that local administration of verapamil was ineffective in suppressing stimulation-induced ACh release, we examined the effects of the intravenous administration of verapamil (300 μg/kg, $n = 6$) on stimulation-induced ACh release in vagotomized animals as a supplemental experiment.

Protocol 3. A 60-min LAD occlusion was performed by using a 3-0 silk suture passed around the LAD just distal to the first diagonal branch. We measured the ACh levels during 45–60 min of ischemia in the absence of Ca^{2+} channel blockade (control, $n = 8$) and examined the effects of verapamil (100 μM, $n = 5$), ω-conotoxin GVIA (10 μM, $n = 5$), and ω-conotoxin MVIIC (10 μM, $n = 5$). A previous result indicated that the ischemia-induced ACh release reached the steady state during 45–60 min of ischemia (14). We also examined the effects of three additional agents, a Na^+/Ca^{2+} exchange inhibitor KB-R7943 (10 μM, $n = 5$) (9, 10), an $Ins(1,4,5)P_3$ receptor blocker xestospongin C (500 μM, $n = 6$) (25), and a nonselective cation channel blocker or a cation-selective stretch activated channel blocker gadolinium (1 mM) (5, 17), on the ischemia-induced ACh release.

Statistical Analysis

All data are presented as mean (SD) values. In *protocol 1*, we compared stimulation-induced ACh release among the five groups using one-way analysis of variance followed by the Student-Neuman-Keuls test (6). In *protocol 2*, we used an unpaired-*t* test (two-sided) to examine the effect of intravenous verapamil administration on stimulation-induced ACh release. In *protocol 3*, we compared ischemia-induced ACh release among the seven groups using one-way analysis of variance followed by the Dunnett' test against the control. For all analyses, differences were considered significant when $P < 0.05$.

RESULTS

In *protocol 1*, the ACh level during electrical vagal stimulation was 22.4 nM (SD 10.6). Local administration of verapamil did not affect stimulation-induced ACh release (Fig. 1). In contrast, local administration of ω-conotoxin GVIA or ω-conotoxin MVIIC suppressed stimulation-induced ACh release. The extent of suppression was greater in the latter. The ACh level was significantly lower in the simultaneous administration group (ω-conotoxin GVIA + ω-conotoxin MVIIC)

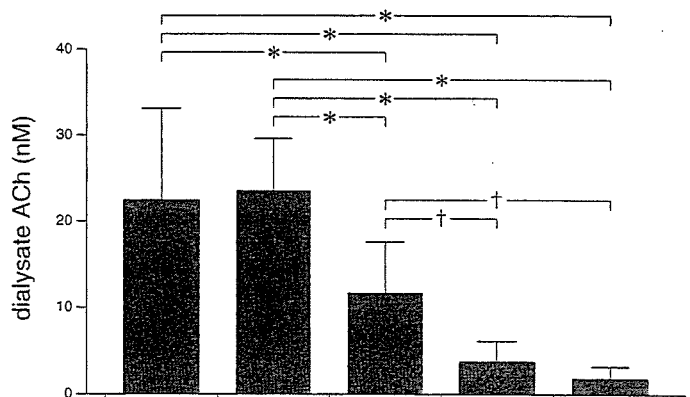

	vehicle	verapamil	ω-CTX GVIA	ω-CTX MVIIC	ω-CTX MVIIC + ω-CTX GVIA
vehicle		0.758	*0.0054*	*0.0002*	*0.0002*
verapamil	0.758		*0.0068*	*0.0002*	*0.0001*
GVIA	*0.0054*	*0.0068*		*0.033*	*0.025*
MVIIC	*0.0002*	*0.0002*	*0.033*		0.581
MVIIC+GVIA	*0.0002*	*0.0001*	*0.025*	0.581	

Fig. 1. Effects of local administration of verapamil, ω-conotoxin GVIA, ω-conotoxin MVIIC, or ω-conotoxin GVIA plus ω-conotoxin MVIIC on vagal nerve stimulation-induced myocardial interstitial ACh release. Both ω-conotoxin GVIA and ω-conotoxin MVIIC, but not verapamil, suppressed stimulation-induced ACh release. Data are mean (SD) values. *$P < 0.01$, †$P < 0.05$. The exact P values are presented.

than that in the ω-conotoxin GVIA group but was not different from the ω-conotoxin MVIIC group.

In *protocol 2*, the intravenous administration of verapamil did not significantly change stimulation-induced ACh release [21.7 nM (SD 12.8)] compared with the control group (P = 0.91).

In *protocol 3*, the ACh level in the ischemic region was 14.9 nM (SD 8.3) during 45–60 min of acute myocardial ischemia. Inhibition of voltage-dependent Ca^{2+} channels by local administration of verapamil, ω-conotoxin GVIA, or ω-conotoxin MVIIC did not affect ischemia-induced ACh release (Fig. 2). Inhibition of the reverse mode action of Na^+/Ca^{2+} exchange by local administration of KB-R7943 appeared to have augmented rather than suppressed ischemia-induced ACh release, though there was no statistically significant difference from the control. Blockade of the $Ins(1,4,5)P_3$ receptor by local administration of xestospongin C did not affect the ischemia-induced ACh release. In contrast, blockade of nonselective cation channels or cation-selective stretch-activated channels by local administration of gadolinium suppressed the ischemia-induced ACh release.

DISCUSSION

Ca^{2+} Channels Involved in Stimulation-Induced ACh Release

Although neurotransmitter release at mammalian sympathetic neuroeffector junctions predominantly depends on Ca^{2+} influx through N-type Ca^{2+} channels (23, 33, 34), the type(s) of Ca^{2+} channels involved in ACh release from cardiac parasympathetic neuroeffector junctions show diversity among reports (8, 28). One possible factor hampering investigations into parasympathetic postganglionic neurotransmitter release in response to vagal nerve stimulation in vivo is that the parasympathetic ganglia are usually situated in the vicinity of the effector organs, thereby making it difficult to separately assess ACh release from preganglionic and postganglionic nerves. In the previous study from our laboratory, intravenous administration, but not local administration of a ganglionic blocker, hexamethonium reduced vagal stimulation-induced ACh release assessed by cardiac microdialysis (1). The negligible effect of local hexamethonium administration on stimulation-induced ACh release suggests the lack of parasympathetic ganglia around the dialysis probe. In support of our speculation, a recent neuroanatomical finding indicates that three ganglia, away from the left anterior free wall targeted by the dialysis probe, provide the major source for left ventricular postganglionic innervation in cats: a cranioventricular ganglion, a left ventricular ganglion 2 (so designated), and an interventriculo-septal ganglion (11). Therefore, ACh, as measured by cardiac microdialysis, is considered to predominantly reflect ACh release from parasympathetic postganglionic nerves.

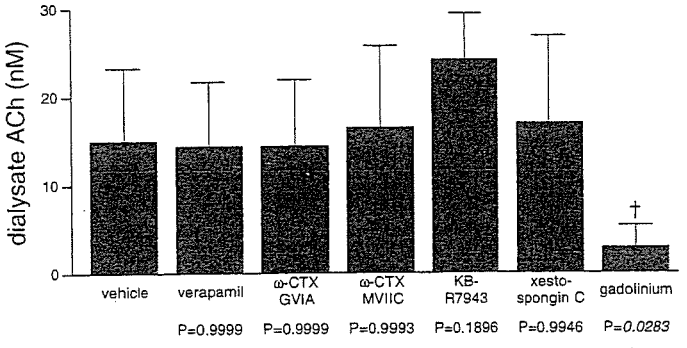

Fig. 2. Effects of local administration of verapamil, ω-conotoxin GVIA, ω-conotoxin MVIIC, KB-R7943, xestospongin C, or gadolinium on acute myocardial ischemia-induced myocardial interstitial ACh release in the ischemic region. Gadolinium alone suppressed the ischemia-induced ACh release. Data are mean (SD) values. †$P < 0.05$. The exact P values are presented.

Local (*protocol 1*) or intravenous (*protocol 2*) administration of verapamil did not affect stimulation-induced ACh release. In contrast, vagal stimulation-induced ACh release was reduced in both the ω-conotoxin GVIA and ω-conotoxin MVIIC groups but to a greater extent in the latter (Fig. 1). Therefore, both N- and P/Q-type, but probably not L-type, Ca^{2+} channels are involved in stimulation-induced ACh release from the cardiac parasympathetic postganglionic nerves in cats. The contribution of P/Q type Ca^{2+} channels to ACh release might be greater than that of N-type Ca^{2+} channels. Hong and Chang (8) reported that the negative inotropic response to field stimulation depends predominantly on the P/Q-type Ca^{2+} channels in isolated guinea pig atria, whereas Serone et al. (28) reported the predominance of N-type Ca^{2+} channels. In those studies, the field stimulation employed differed from ordinary activation of the postganglonic nerves by nerve discharge and, in addition, ACh release was not directly measured. The present study directly demonstrated the involvement of P/Q- and N-type Ca^{2+} channels in the stimulation-induced ACh release in the cardiac parasympathetic postganglionic nerves. These results support the concept that multiple subtypes of the voltage-gated Ca^{2+} channel mediate transmitter release from the same population of parasympathetic neurons (31).

Stimulation-induced ACh release was suppressed by ~50% in the ω-conotoxin GVIA group and by ~80% in the ω-conotoxin MVIIC group. The algebraic summation of the extent of suppression exceeded 100%. The phenomenon may be in part due to the nonlinear dose-response relationship between Ca^{2+} influx and transmitter release (32). The supra-additive phenomenon may be also due to the affinity of ω-conotoxin MVIIC to N-type Ca^{2+} channels (8, 26, 36). Combined local administration of ω-conotoxin GVIA and ω-conotoxin MVIIC almost completely suppressed stimulation-induced ACh release to a level similar to that achieved by the Na^+ channel inhibitor tetrodotoxin (15). Therefore, involvement of another untested type of Ca^{2+} channel(s) is unlikely in the stimulation-induced ACh release from the cardiac parasympathetic postganglionic nerves in cats.

Ca^{2+} Channels and Ischemia-Induced ACh Release

In a previous study, we showed that acute myocardial ischemia evokes myocardial interstitial ACh release in the ischemic region via a local mechanism independent of efferent vagal nerve activity (14). In that study, the inhibition of intracellular Ca^{2+} mobilization by local administration of 3,4,5-trimethoxybenzoic acid 8-(diethyl amino)-octyl ester (TMB-8) suppressed ischemia-induced ACh release, suggesting that an axoplasmic Ca^{2+} elevation is essential for the ischemia-induced ACh release. Because tissue K^+ concentration increases in the ischemic region (7, 18), high K^+-induced

depolarization could activate voltage-dependent Ca^{2+} channels even in the absence of efferent vagal nerve activity. However, ischemia-induced ACh release was not suppressed by local administration of verapamil, ω-conotoxin GVIA, or ω-conotoxin MVIIC (Fig. 2). Therefore, Ca^{2+} entry through the voltage-dependent Ca^{2+} channels is unlikely a mechanism for the ischemia-induced myocardial interstitial ACh release.

Acute myocardial ischemia causes energy depletion in the ischemic region, which impairs Na^+-K^+-ATPase activity. Ischemia also causes acidosis in the ischemic region, which promotes Na^+/H^+ exchange. As a result, ischemia causes intracellular Na^+ accumulation. The decrease in the Na^+ gradient across the plasma membrane may then cause the Na^+/Ca^{2+} exchanger to operate in the reverse mode, facilitating intracellular Ca^{2+} overload. KB-R7943 can inhibit the reverse mode of Na^+/Ca^{2+} exchange (9, 10) and its potential to protect against ischemia-reperfusion injury has been reported (21). In the present study, however, local administration of KB-R7943 failed to suppress and rather increased ACh release during ischemia as opposed to our expectation. It is plausible that the inhibition of reverse mode of Na^+/Ca^{2+} may have facilitated the accumulation of intracellular Na^+ and induced adverse effects that cancelled the possible beneficial effects derived from the inhibition of Ca^{2+} entry through the Na^+/Ca^{2+} exchanger itself. In addition, KB-R7943 could inhibit the forward mode of Na^+/Ca^{2+} exchange and reduce Ca^{2+} efflux (16), contributing to the intracellular Ca^{2+} accumulation and ACh release. In the present study, we observed the effects of KB-R7943 only during the ischemic period. However, accumulation of intracellular Na^+ through Na^+/H^+ exchange is enhanced on reperfusion due to the washout of extracellular H^+ (20). The inhibition of Na^+/Ca^{2+} exchange to suppress Ca^{2+} overload might become more important during the reperfusion phase. For instance, the percent segment shortening of the left ventricle was improved by KB-R7943 during reperfusion but not during ischemia (35).

As already mentioned, the ischemia-induced ACh release can be blocked by TMB-8 and thus the intracellular Ca^{2+} mobilization is required for the ischemia-induced ACh release (14). Besides the Ca^{2+} entries through voltage-dependent Ca^{2+} channels and via the reverse mode of Na^+/Ca^{2+} exchanger, Ca^{2+} may be mobilized from the endoplasmic reticulum via pathological pathways. As an example, the mitochondrial permeability transition pore triggered in pathological conditions is linked to cytochrome *c* release. Cytochrome *c* can bind to the endoplasmic reticulum $Ins(1,4,5)P_3$ receptor, rendering the channel insensitive to autoinhibition by high cytosolic Ca^{2+} concentration and resulting in enhanced endoplasmic reticulum Ca^{2+} release (4, 30). In the present study, however, blockade of $Ins(1,4,5)P_3$ receptor by xestospongin C failed to suppress the ischemia-induced ACh release. In contrast, local administration of gadolinium significantly suppressed the ischemia-induced ACh release. Therefore, nonselective cation channels or cation-selective stretch-activated channels contribute to the ischemia-induced ACh release. During myocardial ischemia, the ischemic region can be subjected to paradoxical systolic bulging. Such bulging likely opens stretch-activated channels and causes myocardial interstitial ACh release, possibly leading to cardioprotection by ACh against ischemic injury (2).

Limitations

First, the experiment was performed under anesthetic conditions, which may have influenced basal autonomic activity. However, because we sectioned the vagi at the neck, basal autonomic activity may have had only a minor effect on ACh release during the vagal stimulation and during acute myocardial ischemia. Second, we added eserine to the perfusate to inhibit immediate degradation of ACh (24), which may have increased the ACh level in the synaptic cleft and activated regulatory pathways such as autoinhibition of ACh release via muscarinic receptors (24). However, the myocardial interstitial ACh level measured under this condition could reflect changes induced by Na^+ channel inhibitor, choline uptake inhibitor, and vesicular ACh transport inhibitor as described in a previous study (15). Therefore, we think that the interpretation of the present results is reasonable. Third, tissue and species differences should be taken into account when extrapolating the present findings, because significant heterogeneity in the Ca^{2+} channels involved in the mammalian parasympathetic system may exist. Finally, we used verapamil to test the involvement of L-type Ca^{2+} channels in the ACh release. There are three major types of L-type Ca^{2+} channel antagonists with different binding domains (verapamil, nifedipine, and diltiazem) (19). Whether the effects on the ACh release are common among the three types of L-type Ca^{2+} channel antagonists remains unanswered.

In conclusion, the N- and P/Q-type Ca^{2+} channels (with the P/Q-type dominant), but probably not the L-type Ca^{2+} channels, are involved in vagal stimulation-induced ACh release from the cardiac parasympathetic postganglionic nerves in cats. In contrast, myocardial interstitial ACh release in the ischemic myocardium is resistant to the blockade of L-, N-, and P/Q-type Ca^{2+} channels. In addition, the ischemia-induced myocardial ACh release is resistant to the inhibition of Na^+/Ca^{2+} exchanger and the blockade of $Ins(1,4,5)P_3$ receptor but is suppressed by gadolinium, suggesting that nonselective cation channels or cation-selective stretch-activated channels are involved.

GRANTS

This study was supported by Health and Labour Sciences Research Grant for Research on Advanced Medical Technology from the Ministry of Health, Labour and Welfare of Japan, Health and Labour Sciences Research Grant for Research on Medical Devices for Analyzing, Supporting and Substituting the Function of Human Body from the Ministry of Health, Labour and Welfare of Japan, Health and Labour Sciences Research Grant H18-Iryo-Ippan-023 from the Ministry of Health, Labour and Welfare of Japan, Program for Promotion of Fundamental Studies in Health Science from the National Institute of Biomedical Innovation, a Grant provided by the Ichiro Kanehara Foundation, Ground-based Research Announcement for Space Utilization promoted by Japan Space Forum, and Industrial Technology Research Grant Program in 03A47075 from New Energy and Industrial Technology Development Organization of Japan.

REFERENCES

1. **Akiyama T, Yamazaki T, and Ninomiya I.** In vivo detection of endogenous acetylcholine release in cat ventricles. *Am J Physiol Heart Circ Physiol* 266: H854–H860, 1994.
2. **Ando M, Katare RG, Kakinuma Y, Zhang D, Yamasaki F, Muramoto K, and Sato T.** Efferent vagal nerve stimulation protects heart against ischemia-induced arrhythmias by preserving connexin43 protein. *Circulation* 112: 164–170, 2005.

3. **Bibevski S and Dunlap ME.** Prevention of diminished parasympathetic control of the heart in experimental heart failure. *Am J Physiol Heart Circ Physiol* 287: H1780–H1785, 2004.
4. **Brookes PS, Yoon Y, Robotham JL, Anders MW, and Sheu SS.** Calcium, ATP, and ROS: a mitochondrial love-hate triangle. *Am J Physiol Cell Physiol* 287: C817–C833, 2004.
5. **Caldwell RA, Clemo HF, and Baumgarten CM.** Using gadolinium to identify stretch-activated channels: technical considerations. *Am J Physiol Cell Physiol* 275: C619–C621, 1998.
6. **Glantz SA.** *Primer of Biostatistics* (5th ed) New York: McGraw-Hill, 2002.
7. **Hirche HJ, Franz CHR, Bös L, Bissig R, Lang R, and Schramm M.** Myocardial extracellular K^+ and H^+ increase and noradrenaline release as possible cause of early arrhythmias following acute coronary artery occlusion in pigs. *J Mol Cell Cardiol* 12: 579–593, 1979.
8. **Hong SJ and Chang CC.** Calcium channel subtypes for the sympathetic and parasympathetic nerves of guinea-pig atria. *Br J Pharmacol* 116: 1577–1582, 1995.
9. **Iwamoto T, Kita S, Uehara A, Inoue Y, Taniguchi Y, Imanaga I, and Shigekawa M.** Structural domains influencing sensitivity to isothiourea derivative inhibitor KB-R7943 in cardiac Na^+/Ca^{2+} exchanger. *Mol Pharmacol* 59: 524–531, 2001.
10. **Iwamoto T, Watano T, and Shigekawa M.** A novel isothiourea derivative selectively inhibits the reverse mode of Na^+/Ca^{2+} exchange in cells expressing NCX1. *J Biol Chem* 271: 22391–22397, 1996.
11. **Johnson TA, Gray AL, Lauenstein JM, Newton SS, and Massari VJ.** Parasympathetic control of the heart. I. An interventriculo-septal ganglion is the major source of the vagal intracardiac innervation of the ventricles. *J Appl Physiol* 96: 2265–2272, 2004.
12. **Kawada T, Yamazaki T, Akiyama T, Inagaki M, Shishido T, Zheng C, Yanagiya Y, Sugimachi M, and Sunagawa K.** Vagosympathetic interactions in ischemia-induced myocardial norepinephrine and acetylcholine release. *Am J Physiol Heart Circ Physiol* 280: H216–H221, 2001.
13. **Kawada T, Yamazaki T, Akiyama T, Li M, Ariumi H, Mori H, Sunagawa K, and Sugimachi M.** Vagal stimulation suppresses ischemia-induced myocardial interstitial norepinephrine release. *Life Sci* 78: 882–887, 2006.
14. **Kawada T, Yamazaki T, Akiyama T, Sato T, Shishido T, Inagaki M, Takaki H, Sugimachi M, and Sunagawa K.** Differential acetylcholine release mechanisms in the ischemic and non-ischemic myocardium. *J Mol Cell Cardiol* 32: 405–414, 2000.
15. **Kawada T, Yamazaki T, Akiyama T, Shishido T, Inagaki M, Uemura K, Miyamoto T, Sugimachi M, Takaki H, and Sunagawa K.** In vivo assessment of acetylcholine-releasing function at cardiac vagal nerve terminals. *Am J Physiol Heart Circ Physiol* 281: H139–H145, 2001.
16. **Kimura J, Watano T, Kawahara M, Sakai E, and Yatabe J.** Direction-independent block of bi-directional Na^+/Ca^{2+} exchange current by KB-R7943 in guinea-ping cardiac myocytes. *Br J Pharmacol* 128: 969–974, 1999.
17. **Kimura S, Mieno H, Tamaki K, Inoue M, and Chayama K.** Nonselective cation channel as a Ca^{2+} influx pathway in pepsinogen-secreting cells of bullfrog esophagus. *Am J Physiol Gastrointest Liver Physiol* 281: G333–G341, 2001.
18. **Kléber AG.** Extracellular potassium accumulation in acute myocardial ischemia. *J Mol Cell Cardiol* 16: 389–394, 1984.
19. **Kurokawa J, Adachi-Akahane S, and Nagao T.** 1–5-Benzothiazepine binding domain is located on the extracellular side of the cardiac L-type Ca^{2+} channel. *Mol Pharmacol* 51: 262–268, 1997.
20. **Lazdunski M, Frelin C, and Vigne P.** The sodium/hydrogen exchange system in cardiac cells: its biochemical and pharmacological properties and its role in regulating internal concentrations of sodium and internal pH. *J Mol Cell Cardiol* 17: 1029–1042, 1985.
21. **Lee C, Dhalla NS, and Hryshko LV.** Therapeutic potential of novel Na^+-Ca^{2+} exchange inhibitors in attenuating ischemia-reperfusion injury. *Can J Cardiol* 21: 509–516, 2005.
22. **Li M, Zheng C, Sato T, Kawada T, Sugimachi M, and Sunagawa K.** Vagal nerve stimulation markedly improves long-term survival after chronic heart failure in rats. *Circulation* 109: 120–124, 2004.
23. **Molderings GJ, Likungu J, and Göthert M.** N-type calcium channels control sympathetic neurotransmission in human heart atrium. *Circulation* 101: 403–407, 2000.
24. **Nicholls DG.** *Proteins, Transmitters and Synapses*. Oxford: Blackwell Science, 1994.
25. **Oka T, Sato K, Hori M, Ozaki H, and Karaki H.** Xestospongin C, a novel blocker of IP_3 receptor, attenuates the increase in cytosolic calcium level and degranulation that is induced by antigen in RBL-2H3 mast cells. *Br J Pharmacol* 135: 1959–1966, 2002.
26. **Randall A and Tsien RW.** Pharmacological dissection of multiple types of Ca^{2+} channel currents in rat cerebellar granule neurons. *J Neurosci* 15: 2995–3012, 1995.
27. **Schauerte P, Scherlag BJ, Scherlag MA, Goli S, Jackman WM, and Lazzara R.** Ventricular rate control during atrial fibrillation by cardiac parasympathetic nerve stimulation: a transvenous approach. *J Am Coll Cardiol* 34: 2043–2050, 1999.
28. **Serone AP and Angus JA.** Role of N-type calcium channels in autonomic neurotransmission in guinea-pig isolated left atria. *Br J Pharmacol* 127: 927–934, 1999.
29. **Smith AB, Motin L, Lavidis NA, and Adams DJ.** Calcium channels controlling acetylcholine release from preganglionic nerve terminals in rat autonomic ganglia. *Neuroscience* 95: 1121–1127, 2000.
30. **Verkhratsky A and Toescu EC.** Endoplasmic reticulum Ca^{2+} homeostasis and neuronal death. *J Cell Mol Med* 4: 351–361, 2003.
31. **Waterman SA.** Multiple subtypes of voltage-gated calcium channel mediate transmitter release from parasympathetic neurons in the mouse bladder. *J Neurosci* 16: 4155–4161, 1996.
32. **Wheeler DB, Randall A, and Tsien RW.** Changes in action potential duration after reliance of excitatory synaptic transmission on multiple types of Ca^{2+} channels in rat hippocampus. *J Neurosci* 16: 2226–2237, 1996.
33. **Yahagi N, Akiyama T, and Yamazaki T.** Effects of ω-conotoxin GVIA on cardiac sympathetic nerve function. *J Auton Nerv Syst* 68: 43–48, 1998.
34. **Yamazaki T, Akiyama T, Kitagawa H, Takauchi Y, Kawada T, and Sunagawa K.** A new, concise dialysis approach to assessment of cardiac sympathetic nerve terminal abnormalities. *Am J Physiol Heart Circ Physiol* 272: H1182–H1187, 1997.
35. **Yoshitomi O, Akiyama D, Hara T, Cho S, Tomiyasu S, and Sumikawa K.** Cardioprotective effects of KB-R7943, a novel inhibitor of Na^+/Ca^{2+} exchanger, on stunned myocardium in anesthetized dogs. *J Anesth* 19: 124–130, 2005.
36. **Zhang JF, Randall AD, Ellinor PT, Horne WA, Sather WA, Tanabe T, Schwarz TL, and Tsien RW.** Distinctive pharmacology and kinetics of cloned neuronal Ca^{2+} channels and their possible counterparts in mammalian CNS neurons. *Neuropharmacology* 32: 1075–1088, 1993.

Reprinted from

MAY 16, 2006
VOLUME 47, NO. 10

JACC

JOURNAL *of the* AMERICAN COLLEGE *of* CARDIOLOGY

Cellular Basis for Trigger and Maintenance of Ventricular Fibrillation in the Brugada Syndrome Model

High-Resolution Optical Mapping Study

Takeshi Aiba, MD, PHD, Wataru Shimizu, MD, PHD, Ichiro Hidaka, MS, Kazunori Uemura, MD, Takashi Noda, MD, PHD, Can Zheng, PHD, Atsunori Kamiya, MD, Masashi Inagaki, MD, Masaru Sugimachi, MD, PHD, Kenji Sunagawa, MD, PHD

ELSEVIER

Journal of the American College of Cardiology
© 2006 by the American College of Cardiology Foundation
Published by Elsevier Inc.

Vol. 47, No. 10, 2006
ISSN 0735-1097/06/$32.00
doi:10.1016/j.jacc.2005.12.064

PRECLINICAL STUDIES

Cellular Basis for Trigger and Maintenance of Ventricular Fibrillation in the Brugada Syndrome Model

High-Resolution Optical Mapping Study

Takeshi Aiba, MD, PHD,* Wataru Shimizu, MD, PHD,† Ichiro Hidaka, MS,* Kazunori Uemura, MD,* Takashi Noda, MD, PHD,* Can Zheng, PHD,* Atsunori Kamiya, MD,* Masashi Inagaki, MD,* Masaru Sugimachi, MD, PHD,* Kenji Sunagawa, MD, PHD*

Suita, Japan

OBJECTIVES We examined how repolarization and depolarization abnormalities contribute to the development of extrasystoles and subsequent ventricular fibrillation (VF) in a model of the Brugada syndrome.

BACKGROUND Repolarization and depolarization abnormalities have been considered to be mechanisms of the coved-type ST-segment elevation (Brugada-electrocardiogram [ECG]) and development of VF in the Brugada syndrome.

METHODS We used high-resolution (256 × 256) optical mapping techniques to study arterially perfused canine right ventricular wedges (n = 20) in baseline and in the Brugada-ECG produced by administration of terfenadine (5 μmol/l), pinacidil (2 μmol/l), and pilsicainide (5 μmol/l). We recorded spontaneous episodes of phase 2 re-entrant (P2R)-extrasystoles and subsequent self-terminating polymorphic ventricular tachycardia (PVT) or VF under the Brugada-ECG condition and analyzed the epicardial conduction velocity and action potential duration (APD) restitutions in each condition.

RESULTS Forty-one episodes of spontaneous P2R-extrasystoles in the Brugada-ECG were successfully mapped in 9 of 10 preparations, and 33 of them were originated from the maximum gradient of repolarization (GR_{max}: 176 ± 54 ms/mm) area in the epicardium, leading to PVT (n = 12) or VF (n = 5). The epicardial GR_{max} was not different between PVT and VF. Wave-break during the first P2R-extrasystole produced multiple wavelets in all VF cases, whereas no wave-break or wave-break followed by wave collision and termination occurred in PVT cases. Moreover, conduction velocity restitution was shifted lower and APD restitution was more variable in VF cases than in PVT cases.

CONCLUSIONS Steep repolarization gradient in the epicardium but not endocardium develops P2R-extrasystoles in the Brugada-ECG condition, which might degenerate into VF by further depolarization and repolarization abnormalities. (J Am Coll Cardiol 2006;47:2074–85)

Brugada syndrome is characterized by ST-segment elevation in the right precordial leads (V_1 to V_3) of electrocardiography (ECG) and a high incidence of ventricular fibrillation (VF) leading to sudden cardiac death (1–4). However, not all of the patients with ST-segment elevation have arrhythmic events (5,6), indicating that additional factors might contribute to development of VF. Previous studies suggest that an accentuation of transient outward potassium current (I_{to})-mediated phase 1 notch and loss of action potential (AP) dome in some areas of the right ventricular (RV) epicardium but not endocardium increases transmural dispersion of repolarization (DR), which causes the ST-segment elevation (7–11). The heterogeneous loss of AP dome in the epicardium also increases epicardial DR, and a propagation of AP dome from a site where AP dome is restored to a site where it is lost might develop a local re-excitation called a phase 2 re-entry (P2R), which triggers a circus movement re-entry in the form of VF (8,9,12). It is still unclear, however, to what extent the epicardial DR is required for development of P2R and how phase 2 re-entrant (P2R)-extrasystoles produce VF. Moreover, depolarization abnormality is thought to be one of the potent arrhythmic substrate in the Brugada syndrome (13–17), but it is not fully understood how depolarization and repolar-

From the *Department of Cardiovascular Dynamics, Research Institute, and the †Division of Cardiology, Department of Internal Medicine, National Cardiovascular Center, Suita, Japan. This work was supported by grants from Japan Cardiovascular Research Foundation (Dr. Aiba) and the Japan Foundation of Cardiovascular Research (Dr. Aiba), Health Sciences Research grants from the Ministry of Health, Labour, and Welfare (Dr. Shimizu), Research grants for Cardiovascular Diseases (15C-6) from the Ministry of Health, Labour, and Welfare (Dr. Shimizu), Japan Science and Technology Agency (Dr. Sunagawa), and a Health and Labour Sciences Research grant for research on medical devices for analyzing, supporting, and substituting the function of the human body from the Ministry of Health Labour, and Welfare of Japan (Dr. Sunagawa). Presented in part at the Scientific Session of the American Heart Association, November 7–10, 2004, and published in abstract form (Circulation 2004;110 Suppl III:III318).

Manuscript received November 10, 2005; revised manuscript received November 25, 2005, accepted December 13, 2005.

Abbreviations and Acronyms

AP	= action potential
APD	= action potential duration
APD_{50}	= action potential duration measured at 50% repolarization
BCL	= basic cycle length
Brugada-ECG	= coved-type ST-segment elevation
Delta-Epi interval	= interval from the earliest to the latest epicardial activation
DR	= dispersion of repolarization
ECG	= electrocardiogram/electrocardiography
GR_{max}	= maximum gradient of repolarization
I_{Ca}	= inward calcium current
$I_{K\text{-}ATP}$	= ATP-sensitive potassium current
I_{Na}	= sodium current
I_{to}	= transient outward potassium current
P2R	= phase 2 re-entrant/entry
RV	= right ventricle/ventricular
Sti-Epi interval	= interval from the stimulus to the earliest epicardial activation
VF	= ventricular fibrillation
VT	= ventricular tachycardia

ization abnormalities interact and contribute to the development and maintenance of VF in the Brugada syndrome.

To investigate the heterogeneities of cellular repolarization and depolarization and their potential role in the development of re-entrant arrhythmias, we used a technique of high-resolution optical mapping, which allowed us to measure the electrical heterogeneity of APs on the epicardial or endocardial surface (18). We demonstrated that a steep repolarization gradient in the RV epicardium but not in the endocardium plays a key role in initiating P2R. Moreover, further depolarization and repolarization abnormalities degenerate the P2R-induced spiral re-entry into multiple wavelets forming VF in an experimental model of the Brugada syndrome.

METHODS

Canine RV wedge model of the Brugada syndrome. All animal care procedures were in accordance with the position of the American Heart Association research animal use (November 11, 1984). The methods used for isolation, perfusion, and recording of transmembrane activity from the arterially perfused canine RV (anterior wall) is similar to methods reported with canine wedge preparations (8,9). Briefly, a transmural wedge with dimensions of approximately 2 × 1 × 0.7 cm to 3 × 1.5 × 1 cm was dissected from the free wall of the RV of male dogs (n = 20), cannulated via the branch of right coronary artery, and placed in a small tissue bath. These preparations were arterially perfused between 40 and 60 mm Hg with Tyrode's solution (35 ± 1°C). The inward calcium current (I_{Ca}) and sodium current (I_{Na}) block with terfenadine (5 μmol/l), combined with augmentation of ATP-sensitive potassium current ($I_{K\text{-}ATP}$) with pinacidil (2 μmol/l), and I_{Na} block with pilsicainide (5 μmol/l) were used to create an experimental model of the Brugada syndrome (8–10,19).

After changing ECG to the coved-type ST-segment elevation mimicking the Brugada syndrome (Brugada-ECG) by administration of these drugs, 1) we recorded the spontaneous occurrence of closely coupled extrasystoles and subsequent non-sustained polymorphic VT (terminated within 5 s) or VF (sustained more than 5 s) during pacing from the endocardium at basic cycle length (BCL) of 2,000 ms (n = 10), and 2) we analyzed restitutions of the epicardial conduction velocity and action potential variable with a single extra stimulus (S2) delivered after every 10th basic beat (S1) paced from the epicardial surface at BCL of 1,000 ms (n = 10).

Transmembrane AP and ECG recording. A transmural ECG was recorded with Ag-AgCl electrodes, which were placed in the Tyrode's solution bathing the preparation, 1.0 cm from the epicardial and endocardial surfaces (epicardial, positive pole). The epicardial and endocardial APs were simultaneously recorded from the epicardial and endocardial surfaces with separate intracellular floating microelectrodes (direct current resistance 10 to 20 MΩ; 2.7 mmol/l potassium chloride) at positions approximating the transmural axis of the ECG.

Optical AP recording. After staining with the voltage sensitive dye, di-4-ANEPPS (5 μmol/l for 30 min), wedges were stabilized against a flat imaging window. Excitation of the dye's fluorescence was achieved with 480 ± 15 nm light through a bandpass filter (ANDV8247, Andover, Salem, New Hampshire) from a bluish-green emission diode (E1L51-3B0A4-02, Toyoda Gosei, Aichi, Japan). Fluoresced light from the wedge was split by a dichrotic mirror and narrowed down to the two frequency bands (approximately 540 or 690 nm) through a bandpass filter (ANDV8368 or ANDV7845, respectively, Andover). Then, the dual-wavelength lights were simultaneously focused onto 10-bit 256 × 256 element dual complementary metal oxide semiconductor (C-MOS) censors (Hamamatsu Photonics, Hamamatsu, Japan) with image intensifiers (FASTCAM-Ultima, Photron, Tokyo, Japan) at a 500 frames/s (Fig. 1).

Both optical signals were digitized at 0.5 kHz, and other amplified signals were digitized at 2 kHz with a 12-bit analog-to-digital converter, stored on the hard disk of a dedicated laboratory computer system, and analyzed with the original software of our laboratory. Therefore, after ratiometry of both signals to subtract a motion artifact, the voltage of the optical signal recorded at each site was automatically displayed in color (lowest, black; greatest, red) and plotted in the 256 × 256 matrix as an isopotential map, and transmembrane APs from 256 sites (16 × 16 units) on the RV epicardial or endocardial surface were displayed in control and in the Brugada-ECG condition with or without arrhythmic events. Moreover, phase analysis was used to display the pattern of wave propagation and wave-break during ventricular tachyarrhythmias (20,21).

Data analysis. Optical action potential duration (APD) was automatically measured at 50% repolarization (APD_{50}),

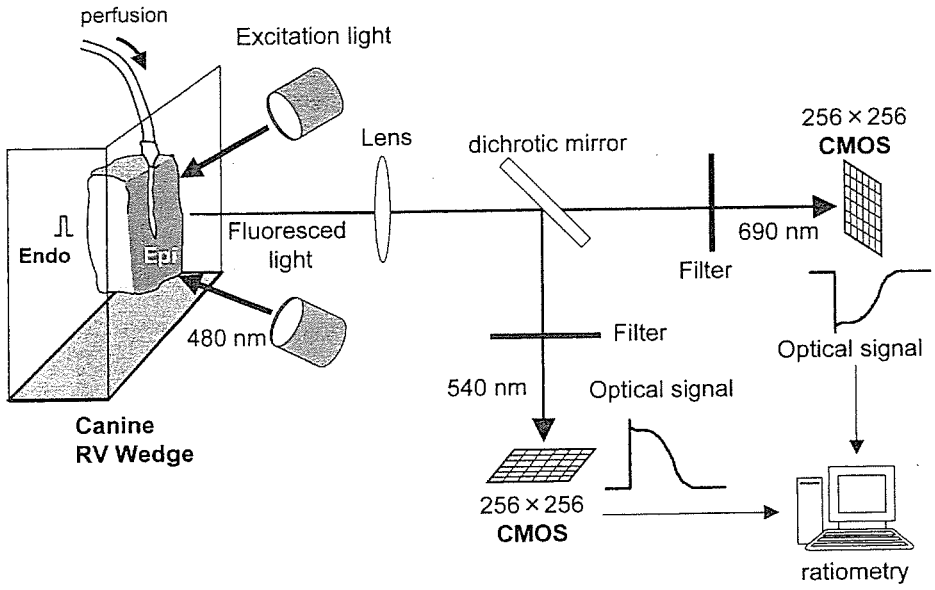

Figure 1. Schematic diagram showing the major components of high-resolution optical mapping of the epicardial (Epi) or endocardial (Endo) surface in an arterially perfused canine right ventricular (RV) wedge preparation. CMOS = complementary metal oxide semiconductor.

and the distributions of epicardial and endocardial APD_{50} were displayed as a repolarization counter map in baseline (control condition) and after changing to the Brugada-ECG with or without P2R-extrasystoles. The epicardial and endocardial DR were calculated from the maximum difference of repolarization times (activation time + APD) in the epicardial and endocardial surfaces, respectively. Transmural DR was calculated from the maximum difference between the epicardial and endocardial repolarization times recorded from the floating microelectrodes. Moreover, the maximum gradient of repolarization (GR_{max} = maximum Delta-APD_{50}/Delta-distance) in the epicardium and endocardium were calculated in each condition. We also measured depolarization parameters such as the interval from the stimulus to the earliest epicardial activation (Sti-Epi interval) and the interval from the earliest to the latest epicardial activation (Delta-Epi interval) during pacing from the endocardium in control and in the Brugada-ECG

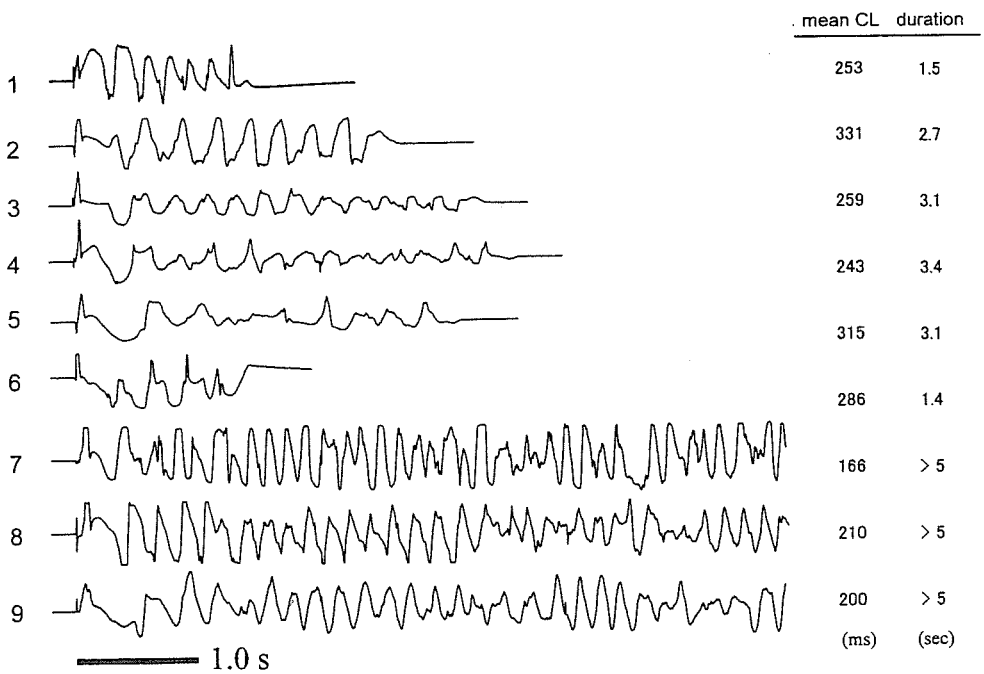

Figure 2. Representative episodes of polymorphic ventricular tachycardia or ventricular fibrillation (VF) in a canine wedge model of the Brugada syndrome. All arrhythmias were spontaneously developed after the electrocardiogram with coved-type ST-segment elevation. Many of the arrhythmias **(numbers 1 to 6)** terminated within a few seconds, but the others **(numbers 7 to 9)** with a shorter cycle length (CL) degenerated into VF, which continued more than 5 s.

condition. Conduction velocity (θ) was determined by linear regression of the isochrone distance versus activation time. Lines parallel and perpendicular to the fiber orientation were defined as the direction of longitudinal (L) and transverse (T) propagation, respectively. The optical data at edge of the preparation, with apparent contraction artifact, and noise level more than 20% of AP amplitude were excluded.

Statistical analysis. Statistical analysis of the data was performed with a Student's t test for paired data or analysis of variance coupled with Scheffe's test, as appropriate. Data is expressed as mean ± SD or mean ± SEM. Significance was defined as a value of $p < 0.05$.

RESULTS

Canine wedge model of the Brugada syndrome. Terfenadine combined with pinacidil and pilsicainide produced the Brugada-ECG in all preparations. There was no arrhythmia in control conditions, whereas combination of the drugs spontaneously developed a P2R-induced short-coupled extrasystole and subsequent polymorphic VT or VF in 9 of 10 preparations (Fig. 2). The QRS interval, QT interval, and J-point level in the ECG were significantly greater in the Brugada-ECG than in the control condition, but those parameters in the Brugada-ECG were not significantly different between beats with and without P2R-extrasystoles (Table 1).

Epicardial repolarization abnormality develops P2R-extrasystoles. Figure 3 represents the epicardial and endocardial APD_{50} contour map and optical APs in the control and in the Brugada-ECG condition with or without P2R-extrasystoles. In the control condition, the epicardial and endocardial APs were almost homogeneous (Figs. 3A and 3D). In contrast, in the Brugada-ECG, the AP morphology in the epicardium but not endocardium changed into heterogeneous, owing to a combination of abbreviated (loss-of-dome) and prolonged (restore-of-dome) APs, resulting in increasing DR in the epicardium rather than in the endocardium (Figs. 3B and 3E). Moreover, further prolonged AP at some areas in the epicardium was closely adjacent to the loss-of-dome APs (arrow), thus producing a repolarization mismatch within a small area and developing a P2R-extrasystole at the loss-of-dome site (Fig. 3C). The APs in the endocardium, however, were less heterogeneous than those in the epicardium even in the Brugada-ECG just before P2R-extrasystoles (Fig. 3F).

The composite data of repolarization and depolarization parameters in the control and in the Brugada-ECG condition with and without P2R-extrasystoles are shown in Table 1. In the Brugada-ECG, the epicardial maximum APD_{50} was significantly prolonged, whereas the epicardial minimum APD_{50} was significantly abbreviated compared with those in the control condition, thus significantly increasing the epicardial DR and GR_{max}. Moreover, the

Table 1. ECG, Repolarization, and Depolarization Parameters in Control and in the Brugada-ECG Condition With or Without Phase 2 Re-Entrant Extrasystoles

		Brugada-ECG	
	Control	P2R-PVC (−)	P2R-PVC (+)
ECG			
QRS duration (ms)	35 ± 4	63 ± 20*	66 ± 22*
QT interval (ms)	286 ± 30	335 ± 33*	—
J-point (mV)	0.04 ± 0.04	0.23 ± 0.08*	0.27 ± 0.08*
Repolarization			
Epicardium			
Max APD_{50} (ms)	239 ± 19	325 ± 86*	480 ± 92*†
Min APD_{50} (ms)	192 ± 16	100 ± 32*	89 ± 28*
Mean APD_{50} (ms)	214 ± 18	200 ± 62	244 ± 68†
DR (ms)	47 ± 11	228 ± 78*	383 ± 93*†
GR_{max} (ms/mm)	5 ± 5	46 ± 29*	176 ± 54*†
Endocardium			
Max APD_{50} (ms)	269 ± 23	269 ± 61	314 ± 77
Min APD_{50} (ms)	214 ± 28	171 ± 53	183 ± 55
Mean APD_{50} (ms)	244 ± 27	219 ± 63	258 ± 70
DR (ms)	56 ± 13	98 ± 44	123 ± 41*
GR_{max} (ms/mm)	8 ± 4	20 ± 13	26 ± 10*
Transmural			
DR (ms)	28 ± 8	135 ± 36*	131 ± 41*
Depolarization			
Sti-Epi interval (ms)	26 ± 10	46 ± 9*	47 ± 12*
Delta-Epi interval (ms)	12 ± 4	19 ± 18	24 ± 20

Values are mean ± SD. *$p < 0.05$ versus control; †$p < 0.05$ versus coved-type ST-segment elevation (Brugada-ECG) condition without P2R-PVC by analysis of variance with Scheffe's test.

APD_{50} = action potential duration at 50% repolarization; Delta-Epi = interval from the earliest to the latest epicardial activation; DR = dispersion of repolarization; GR_{max} = maximum gradient of repolarization; Max = maximum; Min = minimum; P2R-PVC = phase 2 re-entrant extrasystoles; Sti-Epi = interval from the stimulus to the epicardium.

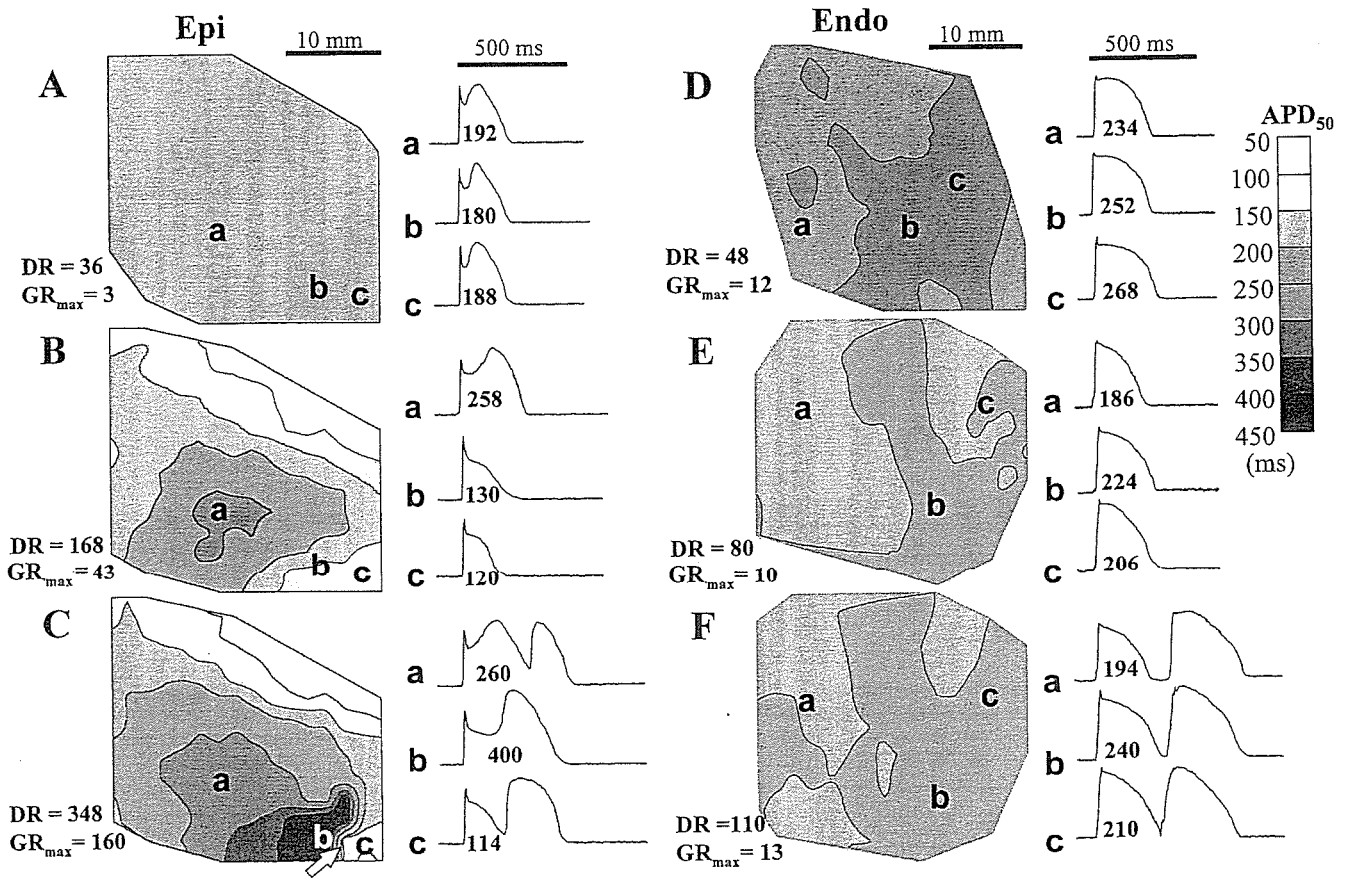

Figure 3. Representative action potential duration measured at 50% repolarization (APD_{50}) contour map on the right ventricular epicardium (Epi) and endocardium (Endo) in control condition (**A and D**, respectively), in the ST-segment elevation (Brugada-ECG) without phase 2 re-entrant (P2R) extrasystoles (**B and E**, respectively), and in the Brugada-ECG just before P2R extrasystoles (**C and F**, respectively) and representative optical action potentials at each site (**a to c**). **White arrow** = initial site of P2R. DR = dispersion of repolarization; GR_{max} = maximum gradient of repolarization.

epicardial maximum APD_{50} was further prolonged in the Brugada-ECG just before P2R-extrasystoles compared with that without P2R-extrasystoles, thus remarkably increasing the epicardial DR and GR_{max}. The endocardial repolarization parameters, however, were not significantly changed after the Brugada-ECG. Moreover, there was no significant difference in the endocardial repolarization parameters between the Brugada-ECG with and without P2R-extrasystoles. Owing to a different response of APD between the epicardium and endocardium, transmural DR was significantly increased in the Brugada-ECG compared with that in the control condition but was not significantly different between the Brugada-ECG condition with and without P2R-extrasystoles.

Regarding depolarization parameters, the Sti-Epi interval was significantly increased in the Brugada-ECG compared with in the control condition but was not different between the condition with and without P2R-extrasystoles. The Delta-Epi interval was not significantly different among the three conditions.

Threshold to develop P2R-extrasystoles. A total of 41 episodes of spontaneous P2R-extrasystoles after the Brugada-ECG were successfully mapped in 9 of 10 preparations, and 33 (80%) of them were originated from the GR_{max} area in the epicardium. As shown in Figure 4, the epicardial GR_{max} was significantly greater in the Brugada-ECG than in control condition. The GR_{max} of 99 ms/mm (dashed line) showed that P2R-extrasystoles were spontaneously developed in the Brugada-ECG. In contrast, the endocardial GR_{max} and transmural DR were greater in the Brugada-ECG condition compared with the control condition but were not different between the Brugada-ECG condition with and without P2R-extrasystoles.

Figure 5A shows the epicardial isopotential map representing the distribution of loss-of-dome and restore-of-dome area in the Brugada-ECG with (beat 2) or without (beat 1) a P2R-extrasystole. Figures 5B and 5C show the depolarization map during the P2R-extrasystole and optical APs at each site on the epicardial surface. At the timing of phase 2 (120 to 190 ms), the restore-of-dome area (orange-red) was larger in the beat 2 than in the beat 1. Moreover, the larger AP dome in the beat 2 moved from a restore-of-dome site (site a and b) to a nearby loss-of-dome site (site d), producing re-excitation at the loss-of-dome site and propagating in a counterclockwise fashion around the refractory region of the epicardium.

P2R-extrasystoles induce polymorphic VT or VF. The epicardial P2R-extrasystoles produced 12 episodes of self-

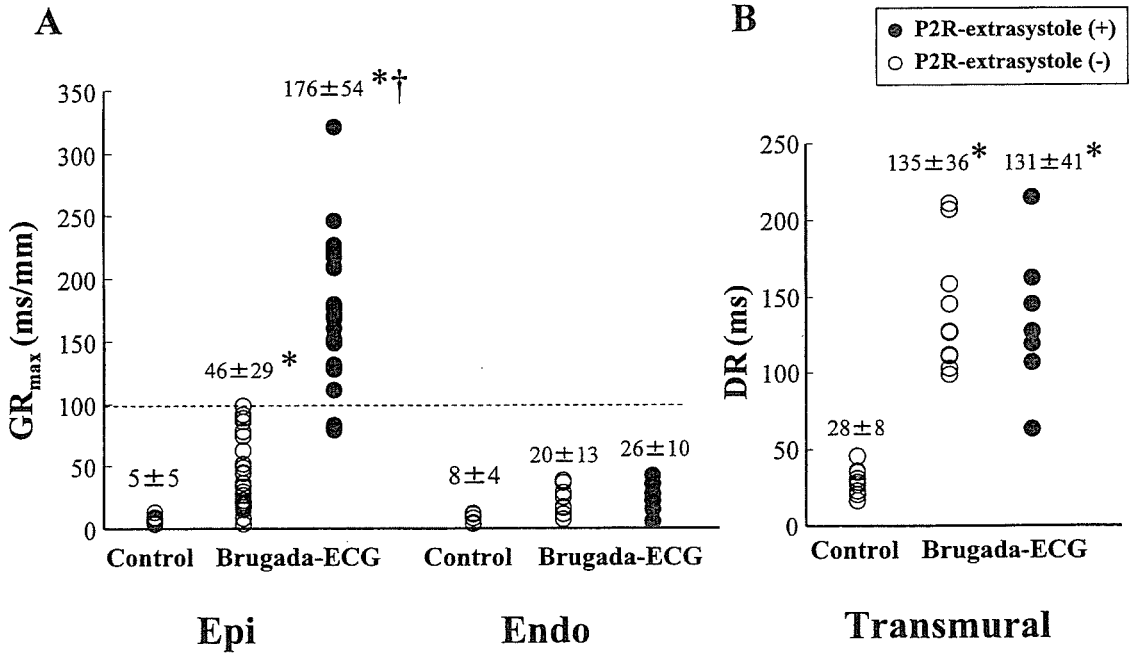

Figure 4. Scatter plots of the maximum gradient of repolarization (GR_{max}) in the epicardial (Epi) and endocardial (Endo) surfaces **(A)** and transmural dispersion of repolarization (DR) **(B)** in control and the ST-segment elevation (Brugada-ECG) condition with **(closed circles)** or without **(open circles)** phase 2 re-entrant (P2R) extrasystoles. Values are mean ± SD. *$p < 0.05$ versus control condition; †$p < 0.05$ versus Brugada-ECG condition without P2R-extrasystole by analysis of variance with Scheffe's test.

terminating (<5 s) polymorphic VT and 5 episodes of sustained (≥5 s) VF. The mechanism underlying the difference between the polymorphic VT and VF is shown in representative examples in Figures 6 and 7. The epicardial GR_{max} area (arrow) developed P2R-extrasystole in both cases (Figs. 6A and 7A); however, the epicardial depolarization map paced from the endocardium at BCL of 2,000 ms shows a remarkable conduction delay in the episode of VF (Fig. 7B) compared with that of polymorphic VT (Fig. 6B). We compared the repolarization and depolarization parameters just before the P2R-induced polymorphic VT and VF in Table 2. There was no significant difference in the repolarization parameters between the two groups; however, the depolarization parameters such as QRS, Sti-Epi, and Delta-Epi intervals were significantly longer in the VF group than in the polymorphic VT group.

Figures 6C and 6D represent phase map and optical APs, respectively, during the P2R-induced polymorphic VT, showing that re-entry was initiated from the epicardial GR_{max} area and rotated mainly in the epicardium without wave-break. In contrast, Figures 7C and 7D represent those during the P2R-induced VF, showing that the development of initial P2R was similar to that of polymorphic VT, but the first P2R-wave was broken up into the multiple wavelets, resulting in degenerating VT into VF. The phase singularity points during the first P2R-wave almost coincided with the sites of delayed conduction (Fig. 7B). In all VF cases, the wave was broken up into multiple wandering wavelets during the first P2R-induced extrasystole; however, in the polymorphic VT cases, only 3 of 12 (25%) cases had a wave-break after the second beat, but soon after the wave had been broken, the waves collided and finally terminated.

Conduction and APD restitutions by S1-S2 method. In another 10 preparations, we analyzed the epicardial conduction velocity and APD restitutions to show the mechanisms underlying the wave-break during the first re-entrant wave in the VF cases. The epicardial longitudinal and transverse conduction velocities (θ_L and θ_T) in the VF cases (n = 5) were significantly slower than those in the polymorphic VT cases (n = 5) under the Brugada-ECG condition, and the conduction velocity restitution curve in the VF cases was shifted lower in parallel (Fig. 8).

In contrast, the epicardial APD was abbreviated and its restitution was flat in the polymorphic VT case under the Brugada-ECG condition, owing to loss of AP dome (Fig. 9B); however, in the VF case, shorter S1-S2 interval (≤300 ms) rather prolonged APD because of restoration of AP dome. Moreover, this restoration was heterogeneous in the epicardial surface, increasing the epicardial DR (Fig. 9C). This "inverse" APD restitution pattern was observed in four of five VF cases but in only one of five polymorphic VT cases under the Brugada-ECG condition.

DISCUSSION

Repolarization mismatch develops P2R-extrasystoles. All-or-none repolarization of the ventricular AP and P2R is considered to be one of the potential mechanism of the ST-segment elevation and subsequent VF in the Brugada

JACC Vol. 47, No. 10, 2006
May 16, 2006:2074–85

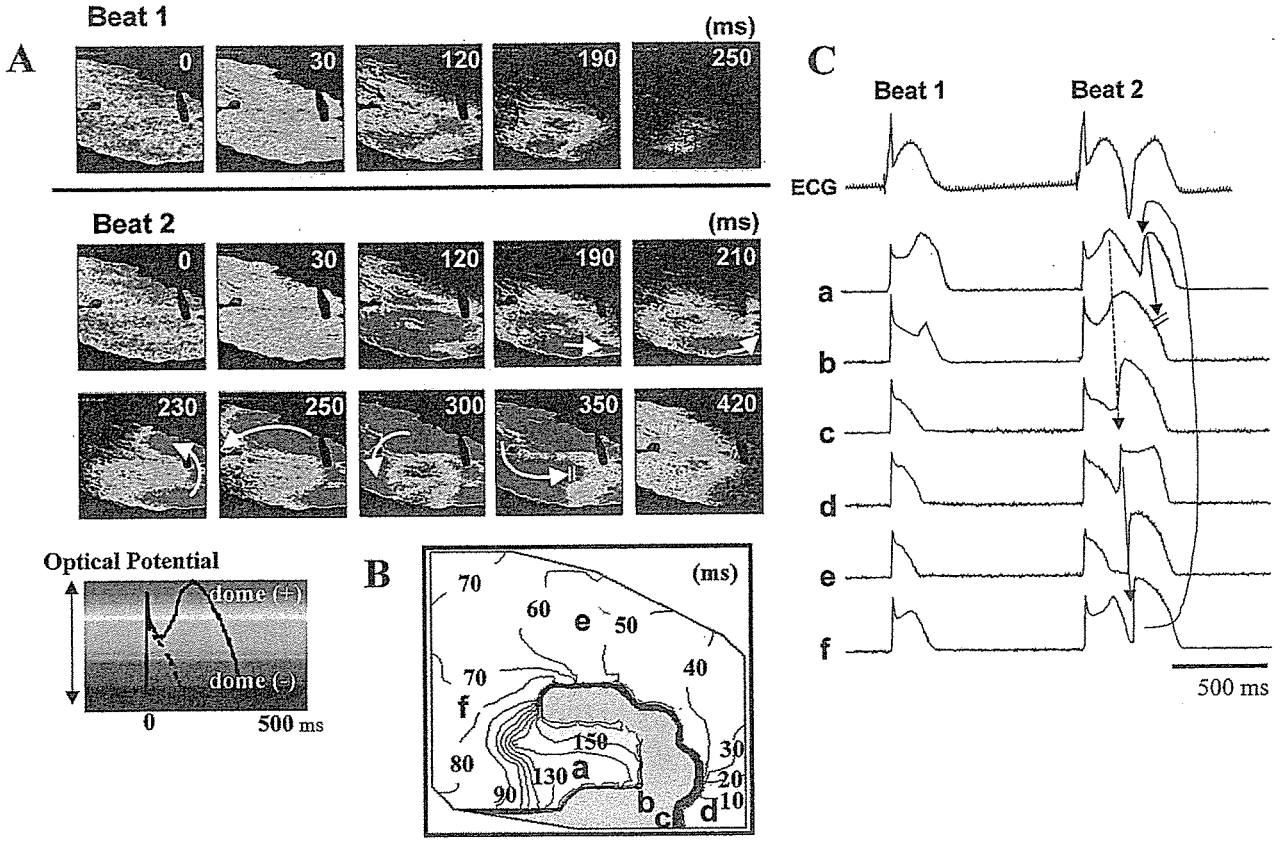

Figure 5. Snapshots of a color optical isopotential movie on the epicardial surface for the continuous two beats with (Beat 2) and without (Beat 1) a phase 2 re-entrant extrasystole (P2R-extrasystole) in the Brugada-ECG condition **(A)**. Depolarization map of a P2R-extrasystole **(B)** and optical action potentials at each site **(a to f)** and transmural electrocardiogram (ECG) **(C)**. Please see the Appendix for accompanying video.

syndrome (7–9,12); however, because of limitations of conventional electrophysiological recording techniques, it remains unknown to what extent the heterogeneity of APs is required for developing P2R-extrasystoles in the Brugada-ECG. In this study, we conducted a high-resolution optical mapping in canine RV wedge preparation, which allowed a detailed measurement of cellular repolarization and depolarization in the epicardial and endocardial surfaces. First, we photographed the moment that P2R-extrasystoles in the Brugada-ECG occurred and produced re-entrant arrhythmias such as polymorphic VT or VF. A unique topographical distribution of both loss-of-dome and restore-of-dome cells in the epicardium but not endocardium might underlie a key feature of the Brugada phenotype, including coved-type ST-segment elevation and susceptibility to P2R-induced ventricular tachyarrhythmias. It must be essential to develop P2R-extrasystoles that further prolong the epicardial AP results in loss-of-dome at some areas but not at the closely adjacent area, making a steep repolarization mismatch. These data are consistent with some clinical reports that the QT interval is more prolonged in the right precordial leads than in other leads during typical coved-type Brugada-ECG (2,13,22) and that VF in the Brugada syndrome was frequently induced by the specific premature ventricular contractions originated from the free wall of RV outflow tract (23,24).

Ionic backgrounds of Brugada-ECG and P2R-extrasystoles. Previous experimental studies pharmacologically created the Brugada-ECG by using various drugs and/or conditions capable of causing an outward shift in the current active at the end of phase 1 of RV epicardium (e.g., increase in I_{to}, $I_{K\text{-}ATP}$, and/or $I_{K\text{-}ACh}$ and decrease in I_{Ca} and I_{Na}) (4,7–10,19). Moreover, a development of P2R on the basis of the all-or-none repolarization phenomenon might depend on a fine balance of I_{to}, I_{Na}, and I_{Ca}. We used block of I_{Ca} and I_{Na} (and other currents) with terfenadine (5 μmol/l), combined with augmentation of $I_{K\text{-}ATP}$ with pinacidil (2 μmol/l) and I_{Na} block with pilsicainide (5 μmol/l); a combination that is most likely to produce the Brugada-ECG. The reason a loss-of-dome occurred in some areas but not others in the epicardium is expected to be owing to an intrinsic difference in I_{to} (25). Miyoshi et al. (26) investigated the mechanism of P2R by their mathematical model and suggested that P2R was developed from a boundary area (0.8 cm) between loss-of-dome and restore-of-dome where a fine balance between I_{to} and $I_{Ca,L}$ was required and that $I_{Ca,L}$ must play an essential role in the genesis of P2R. This mathematical model

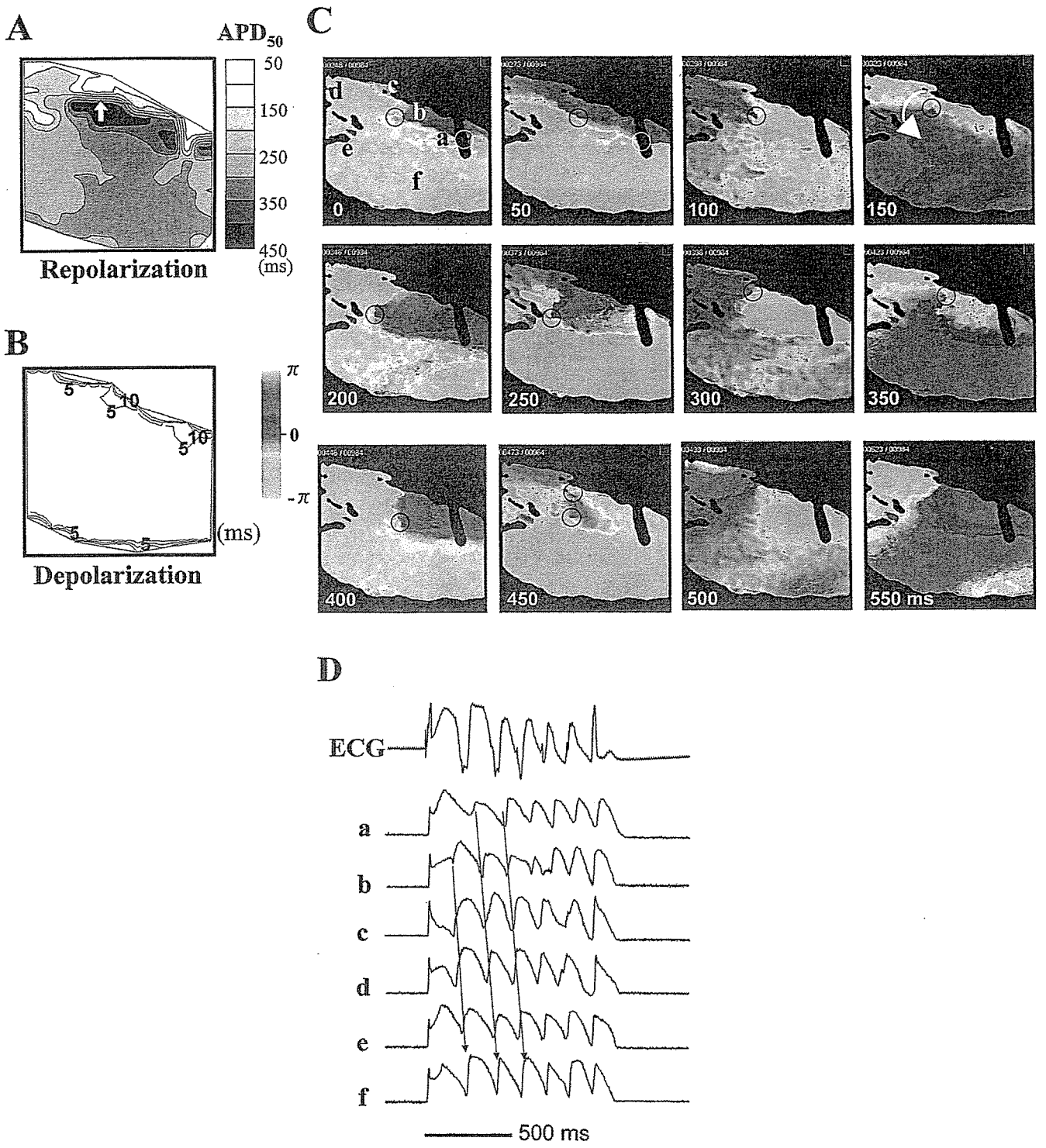

Figure 6. Representative repolarization and depolarization maps on the epicardial surface in the ST-segment elevation (Brugada-ECG) condition just before non-sustained polymorphic ventricular tachycardia (VT) (**A, B**), snapshots of phase movie during polymorphic VT originated from the epicardial phase 2 re-entry (**C**), and optical action potentials at each site (**a to f**) together with a transmural electrocardiogram (ECG) (**D**). **Open circles** = singularity points. APD_{50} = action potential duration at 50% repolarization. Please see the Appendix for accompanying video.

JACC Vol. 47, No. 10, 2006
May 16, 2006:2074–85

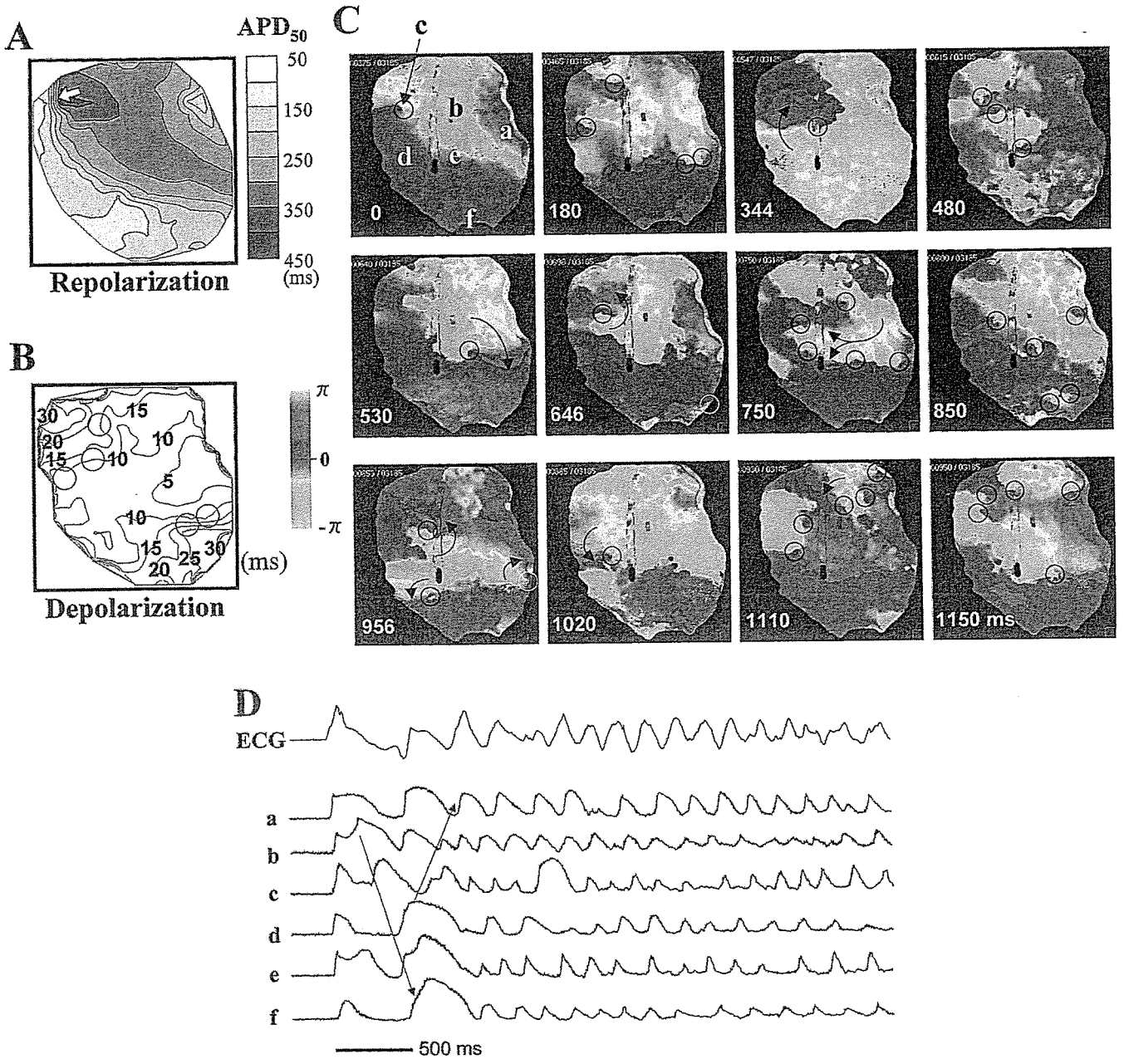

Figure 7. Representative repolarization and depolarization maps on the epicardial surface in the ST-segment elevation (Brugada-ECG) condition just before ventricular fibrillation (VF) **(A, B)**, snapshots of phase movie during VF originated from the epicardial phase 2 re-entry **(C)**, and optical action potentials at each site **(a to f)** together with a transmural electrocardiogram (ECG) **(D)**. **Open circles** = singularity points. APD_{50} = action potential duration at 50% repolarization. Please see the Appendix for accompanying videos.

supports our data that most of P2R-extrasystoles were developed from a small area (<0.5 cm) of GR_{max}.

Maintenance of VF. The only gene linked to the Brugada syndrome is cardiac sodium channel gene, *SCN5A* (17,27). Moreover, sodium channel blockades often unmask Brugada-phenotype, because a loss of sodium channels function enhances both repolarization and depolarization abnormalities (25,28,29). Our experimental study used a pure sodium channel blocker, pilsicainide, to produce the Brugada-ECG associated with prolonged QRS duration and conduction parameters; however, in the Brugada-ECG condition, the depolarization parameters were not different in beats with and without P2R-extrasystoles. In contrast, slower conduction was closely associated with VF susceptibility. These findings suggest that depolarization disturbance was not directly associated with the development of P2R-extrasystole, a trigger of VF, but might contribute to the maintenance of VF in the Brugada-ECG condition.

Electrophysiologic mechanism of VF in the Brugada syndrome has been considered to be re-entry because of high inducibility and reproducibility of VT/VF by pro-

Table 2. ECG, Optical Repolarization, and Depolarization Parameters Just Before Polymorphic VT or VF in the Brugada-ECG Condition

	PVT (n = 12)	VF (n = 5)	p Value
VT/VF CL (ms)	325 ± 33	190 ± 23	<0.001
QRS duration (ms)	74 ± 18	102 ± 23	0.009
J-point (mV)	0.48 ± 0.31	0.43 ± 0.15	NS
Epi max-min APD_{50} (ms)	394 ± 79	344 ± 88	NS
Epi GR_{max} (ms/mm)	169 ± 55	157 ± 22	NS
Sti-Epi interval (ms)	43 ± 10	60 ± 16	0.03
Delta-Epi interval (ms)	13 ± 3	41 ± 16	0.001

Values are mean ± SD.
CL = averaged tachycardia cycle length; PVT = polymorphic ventricular tachycardia; VF = ventricular fibrillation; VT = ventricular tachycardia; other abbreviations as in Table 1.

grammed electrophysiologic stimulation (3,6,14,30), although it is still unclear how VF re-entry is maintained in the Brugada syndrome. In this study, most of the polymorphic VT was single or figure-of-eight type re-entry with no wave-break and terminated within a few seconds (Fig. 6C). In contrast, wave-break in VF group occurred during the first re-entrant wave and took place at sites of the delayed epicardial conduction (Fig. 7B). Wu et al. (31) demonstrated that Ca^{2+} and fast Na^+ current inhibition turned fast VF into slow VF by flattering APD restitution and increasing conduction time. In this Brugada model, however, VF was characterized as the shorter cycle length and multiple wandering wavelets (Fig. 7C) in spite of the slower conduction (Fig. 8), because APD restitution was not flat but rather an "inverse" pattern (Fig. 9), thus increasing dispersion of repolarization during tachycardia. Krishnan and Antzelevitch (25) had demonstrated the incremental arrhythmogenesis of Na^+ channel dysfunction in the RV epicardium during tachycardia. Flecainide also rate-dependently slowed down the conduction velocity. Thus, fast Na^+ current inhibition strongly enhances both heterogeneity of repolarization and conduction slowing during tachycardia in the Brugada-ECG model, which can easily break up the spiral re-entry, thus degenerating polymorphic VT into VF with multiple wavelets.

Clinical implication. Previous clinical study suggested that induction of VF by programmed ventricular stimulation depended on the severity of depolarization abnormalities such as a longer QRS duration or His-ventricular interval but did not predict the recurrence of cardiac events in symptomatic Brugada syndrome (14,15). Moreover, depolarization and repolarization abnormalities in this syndrome are now considered to be closely correlated (16,29,32,33), supporting our data that both repolarization and depolar-

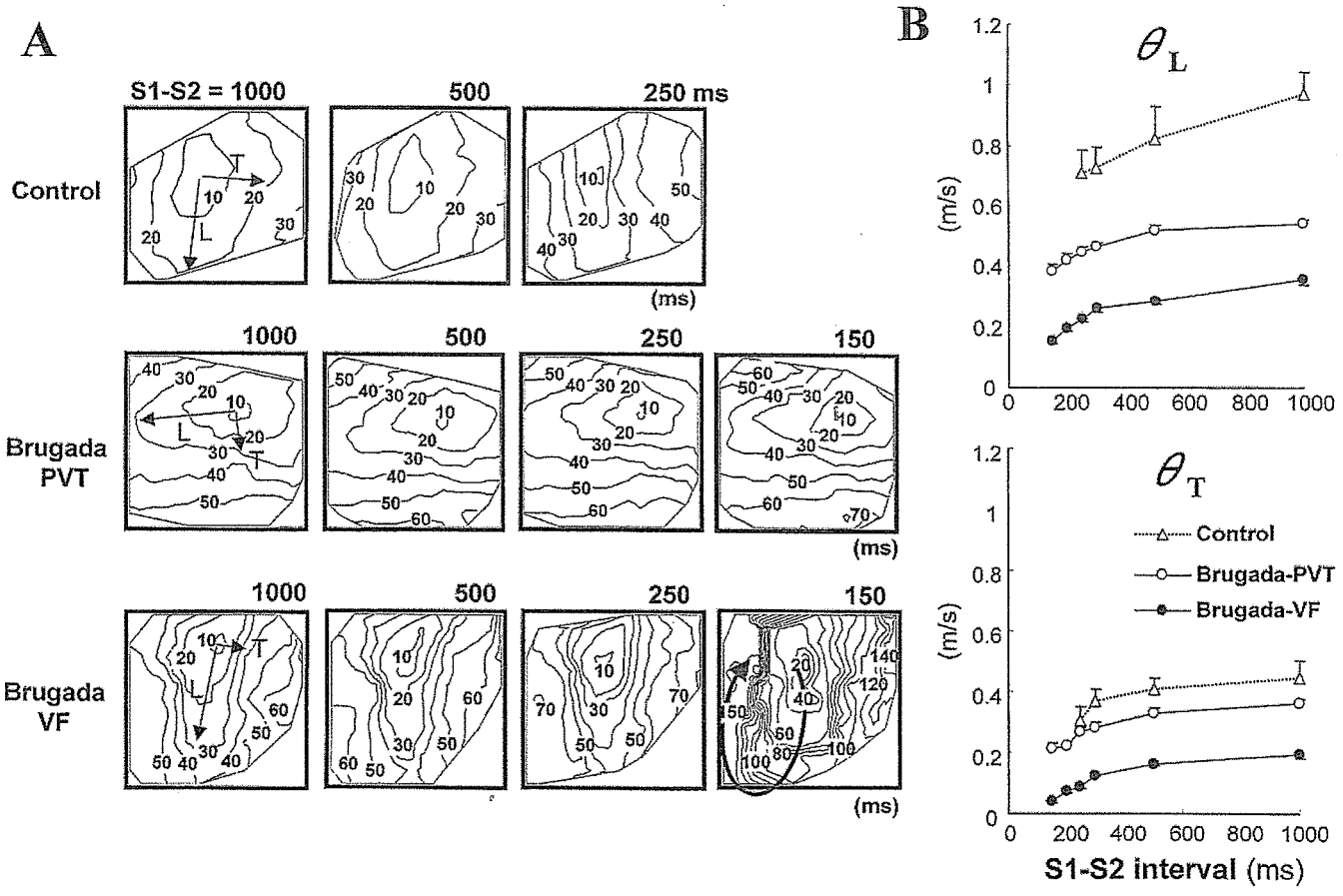

Figure 8. Representative epicardial depolarization maps paced from the epicardium by S1-S2 method in the control and ST-segment elevation (Brugada-ECG) condition with polymorphic ventricular tachycardia (PVT) or ventricular fibrillation (VF) **(A)**, and longitudinal (L) and transverse (T) conduction velocity (θ) restitution curves in each condition **(B)**. Values are mean ± SEM.

JACC Vol. 47, No. 10, 2006
May 16, 2006:2074–85

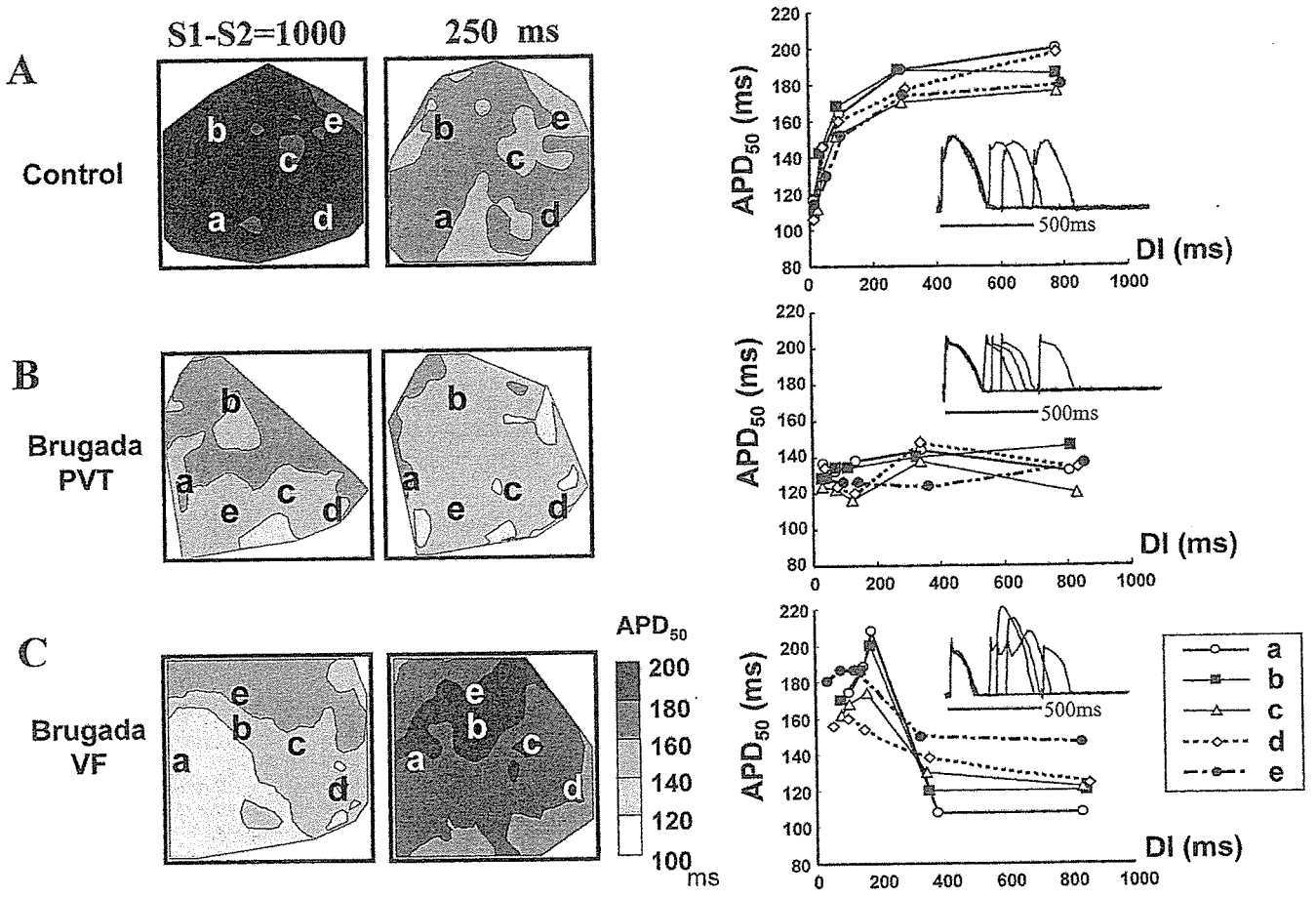

Figure 9. Representative epicardial repolarization maps paced from the epicardium by S1-S2 method and plot of the restitution of action potential duration at each site (**a to e**) and superimposed optical action potentials at site b in control condition (**A**), and the Brugada-ECG condition with polymorphic ventricular tachycardia (PVT) (**B**) or ventricular fibrillation (VF) (**C**). APD_{50} = action potential duration at 50% repolarization; DI = diastolic interval.

ization abnormalities were important in the development of VF. Our results, for the first time, revealed how repolarization and depolarization abnormalities interact in developing a trigger of premature ventricular complexes and in maintaining VF in the Brugada-ECG condition. A steep repolarization gradient in the epicardium introduced P2R-extrasystoles and subsequent non-sustained polymorphic VT, and further increased depolarization and repolarization abnormalities maintained VF, thus increasing risk of sudden cardiac death.

Study limitations. First, we mapped the epicardial or endocardial surface separately in each condition. Therefore, the two-dimensional mapping technique used in this study provides only limited insights into the number of spiral waves and these re-entrant patterns and could not directly evaluate the relationship between the transmural gradient of repolarization and arrhythmogenesis in the Brugada-ECG condition. A second limitation is the size of wedge preparation. It is unclear whether a polymorphic VT or VF in the wedges can result in those with larger hearts. Third, we pharmacologically created, similarly to the methods of previous studies, the Brugada-phenotype, which could not be a complete surrogate for the Brugada syndrome. Finally, with optical mapping, there is a major concern about motion artifacts that can greatly distort the AP recorded, but our ratio-metric methods can reduce motion artifacts without using an uncoupler.

Reprint requests and correspondence: Dr. Wataru Shimizu, Division of Cardiology, Department of Internal Medicine, National Cardiovascular Center, 5-7-1 Fujishiro-dai, Suita, Osaka, 565-8565 Japan. E-mail: wshimizu@hsp.ncvc.go.jp.

REFERENCES

1. Brugada P, Brugada J. Right bundle branch block, persistent ST-segment elevation and sudden cardiac death: a distinct clinical and electrocardiographic syndrome. A multicenter report. J Am Coll Cardiol 1992;20:1391–6.
2. Wilde AA, Antzelevitch C, Borggrefe M, et al. Proposed diagnostic criteria for the Brugada syndrome: consensus report. Circulation 2002; 106:2514–9.
3. Brugada J, Brugada R, Antzelevitch C, Towbin J, Nademanee K, Brugada P. Long-term follow-up of individuals with the electrocardiographic pattern of right bundle-branch block and ST-segment elevation in precordial leads V1 to V3. Circulation 2002;105:73–8.
4. Antzelevitch C, Brugada P, Borggrefe M, et al. Brugada syndrome: report of the second consensus conference: endorsed by the Heart Rhythm Society and the European Heart Rhythm Association. Circulation 2005;111:659–70.
5. Brugada J, Brugada R, Brugada P. Determinants of sudden cardiac death in individuals with the electrocardiographic pattern of Brugada

syndrome and no previous cardiac arrest. Circulation 2003;108: 3092–6.
6. Priori SG, Napolitano C, Gasparini M, et al. Natural history of Brugada syndrome: insights for risk stratification and management. Circulation 2002;105:1342–7.
7. Antzelevitch C, Brugada P, Brugada J, Brugada R, Towbin JA, Nademanee K. Brugada syndrome: 1992–2002: a historical perspective. J Am Coll Cardiol 2003;41:1665–71.
8. Yan GX, Antzelevitch C. Cellular basis for the Brugada syndrome and other mechanisms of arrhythmogenesis associated with ST-segment elevation. Circulation 1999;100:1660–6.
9. Di Diego JM, Cordeiro JM, Goodrow RJ, et al. Ionic and cellular basis for the predominance of the Brugada syndrome phenotype in males. Circulation 2002;106:2004–11.
10. Fish JM, Antzelevitch C. Role of sodium and calcium channel block in unmasking the Brugada syndrome. Heart Rhythm 2004;1:210–7.
11. Kurita T, Shimizu W, Inagaki M, et al. The electrophysiologic mechanism of ST-segment elevation in Brugada syndrome. J Am Coll Cardiol 2002;40:330–4.
12. Lukas A, Antzelevitch C. Phase 2 re-entry as a mechanism of initiation of circus movement re-entry in canine epicardium exposed to simulated ischemia. Cardiovasc Res 1996;32:593–603.
13. Nademanee K, Veerakul G, Nimmannit S, et al. Arrhythmogenic marker for the sudden unexplained death syndrome in Thai men. Circulation 1997;96:2595–600.
14. Kanda M, Shimizu W, Matsuo K, et al. Electrophysiologic characteristics and implications of induced ventricular fibrillation in symptomatic patients with Brugada syndrome. J Am Coll Cardiol 2002;39: 1799–805.
15. Ikeda T, Sakurada H, Sakabe K, et al. Assessment of noninvasive markers in identifying patients at risk in the Brugada syndrome: insight into risk stratification. J Am Coll Cardiol 2001;37:1628–34.
16. Nagase S, Kusano KF, Morita H, et al. Epicardial electrogram of the right ventricular outflow tract in patients with the Brugada syndrome: using the epicardial lead. J Am Coll Cardiol 2002;39:1992–5.
17. Smits JP, Eckardt L, Probst V, et al. Genotype-phenotype relationship in Brugada syndrome: electrocardiographic features differentiate SCN5A-related patients from non-SCN5A-related patients. J Am Coll Cardiol 2002;40:350–6.
18. Akar FG, Spragg DD, Tunin RS, Kass DA, Tomaselli GF. Mechanisms underlying conduction slowing and arrhythmogenesis in nonischemic dilated cardiomyopathy. Circ Res 2004;95:717–25.
19. Kimura M, Kobayashi T, Owada S, et al. Mechanism of ST elevation and ventricular arrhythmias in an experimental Brugada syndrome model. Circulation 2004;109:125–31.
20. Gray RA, Pertsov AM, Jalife J. Spatial and temporal organization during cardiac fibrillation. Nature 1998;392:75–8.
21. Liu YB, Peter A, Lamp ST, Weiss JN, Chen PS, Lin SF. Spatiotemporal correlation between phase singularities and wavebreaks during ventricular fibrillation. J Cardiovasc Electrophysiol 2003;14:1103–9.
22. Pitzalis MV, Anaclerio M, Iacoviello M, et al. QT-interval prolongation in right precordial leads: an additional electrocardiographic hallmark of Brugada syndrome. J Am Coll Cardiol 2003;42:1632–7.
23. Kakishita M, Kurita T, Matsuo K, et al. Mode of onset of ventricular fibrillation in patients with Brugada syndrome detected by implantable cardioverter defibrillator therapy. J Am Coll Cardiol 2000;36: 1646–53.
24. Morita H, Fukushima-Kusano K, Nagase S, et al. Site-specific arrhythmogenesis in patients with Brugada syndrome. J Cardiovasc Electrophysiol 2003;14:373–9.
25. Krishnan SC, Antzelevitch C. Flecainide-induced arrhythmia in canine ventricular epicardium. Phase 2 re-entry? Circulation 1993;87: 562–72.
26. Miyoshi S, Mitamura H, Fujikura K, et al. A mathematical model of phase 2 re-entry: role of L-type Ca current. Am J Physiol Heart Circ Physiol 2003;284:H1285–94.
27. Chen Q, Kirsch GE, Zhang D, et al. Genetic basis and molecular mechanism for idiopathic ventricular fibrillation. Nature 1998;392: 293–6.
28. Brugada R, Brugada J, Antzelevitch C, et al. Sodium channel blockers identify risk for sudden death in patients with ST-segment elevation and right bundle branch block but structurally normal hearts. Circulation 2000;101:510–5.
29. Shimizu W, Antzelevitch C, Suyama K, et al. Effect of sodium channel blockers on ST segment, QRS duration, and corrected QT interval in patients with Brugada syndrome. J Cardiovasc Electrophysiol 2000; 11:1320–9.
30. Gasparini M, Priori SG, Mantica M, et al. Programmed electrical stimulation in Brugada syndrome: how reproducible are the results? J Cardiovasc Electrophysiol 2002;13:880–7.
31. Wu TJ, Lin SF, Weiss JN, Ting CT, Chen PS. Two types of ventricular fibrillation in isolated rabbit hearts: importance of excitability and action potential duration restitution. Circulation 2002;106: 1859–66.
32. Hisamatsu K, Kusano KF, Morita H, et al. Relationships between depolarization abnormality and repolarization abnormality in patients with Brugada syndrome. J Cardiovasc Electrophysiol 2004;15:870–6.
33. Tukkie R, Sogaard P, Vleugels J, de Groot IK, Wilde AA, Tan HL. Delay in right ventricular activation contributes to Brugada syndrome. Circulation 2004;109:1272–7.

APPENDIX

For accompanying videos to Figures 5, 6, and 7, please see the online version of this article.

Am J Physiol Heart Circ Physiol 291: H318–H326, 2006.
First published February 24, 2006; doi:10.1152/ajpheart.00975.2005.

Short-term electroacupuncture at Zusanli resets the arterial baroreflex neural arc toward lower sympathetic nerve activity

Daisaku Michikami,[1,2] Atsunori Kamiya,[1] Toru Kawada,[1] Masashi Inagaki,[1] Toshiaki Shishido,[1] Kenta Yamamoto,[1,2] Hideto Ariumi,[1,2] Satoshi Iwase,[3] Junichi Sugenoya,[3] Kenji Sunagawa,[4] and Masaru Sugimachi[1]

[1]*Department of Cardiovascular Dynamics, Advanced Medical Engineering Center, National Cardiovascular Center Research Institute, Osaka;* [2]*Pharmaceuticals and Medical Devices Agency, Tokyo;* [3]*Department of Physiology, School of Medicine Aichi Medical University, Nagakute, Aichi; and* [4]*Department of Cardiovascular Medicine, Kyushu University Graduate School of Medical Sciences, Fukuoka, Japan*

Submitted 12 September 2005; accepted in final form 17 February 2006

Michikami, Daisaku, Atsunori Kamiya, Toru Kawada, Masashi Inagaki, Toshiaki Shishido, Kenta Yamamoto, Hideto Ariumi, Satoshi Iwase, Junichi Sugenoya, Kenji Sunagawa, and Masaru Sugimachi. Short-term electroacupuncture at Zusanli resets the arterial baroreflex neural arc toward lower sympathetic nerve activity. *Am J Physiol Heart Circ Physiol* 291: H318–H326, 2006. First published February 24, 2006; doi:10.1152/ajpheart.00975.2005.—Although electroacupuncture reduces sympathetic nerve activity (SNA) and arterial pressure (AP), the effects of electroacupuncture on the arterial baroreflex remain to be systematically analyzed. We investigated the effects of electroacupuncture of Zusanli on the arterial baroreflex using an equilibrium diagram comprised of neural and peripheral arcs. In anesthetized, vagotomized, and aortic-denervated rabbits, we isolated carotid sinuses and changed intra-carotid sinus pressure (CSP) from 40 to 160 mmHg in increments of 20 mmHg/min while recording cardiac SNA and AP. Electroacupuncture of Zusanli was applied with a pulse duration of 5 ms and a frequency of 1 Hz. An electric current 10 times the minimal threshold current required for visible muscle twitches was used and was determined to be 4.8 ± 0.3 mA. Electroacupuncture for 8 min decreased SNA and AP (n = 6). It shifted the neural arc (i.e., CSP-SNA relationship) to lower SNA but did not affect the peripheral arc (i.e., SNA-AP relationship) (n = 8). SNA and AP at the closed-loop operating point, determined by the intersection of the neural and peripheral arcs, decreased from 100 ± 4 to 80 ± 9 arbitrary units and from 108 ± 9 to 99 ± 8 mmHg (each $P < 0.005$), respectively. Peroneal denervation eliminated the shift of neural arc by electroacupuncture (n = 6). Decreasing the pulse duration to <2.5 ms eliminated the effects of SNA and AP reduction. In conclusion, short-term electroacupuncture resets the neural arc to lower SNA, which moves the operating point toward lower AP and SNA under baroreflex closed-loop conditions.

arterial pressure; equilibrium diagram

ALTHOUGH THERE ARE MANY clinical case reports (21, 30, 32, 39, 40, 42), the effects of electroacupuncture on cardiovascular regulation remain to be systematically investigated. There has been a recent renewal of interest in the inhibitory effects of electroacupuncture of the Zusanli acupoint on the cardiovascular system, including reductions in arterial pressure (AP), heart rate, (3, 15, 16), and sympathetic nerve activity (SNA) (25, 42). Such inhibitory effects are observed during low-frequency (<20 Hz) electroacupuncture. Because the arterial baroreflex is one of the most important control systems that stabilize AP, we quantified the effects of electroacupuncture on the arterial baroreflex over an entire operating range. Systematic analysis would help to assess the possible utility of electroacupuncture as a treatment modality for certain cardiovascular diseases with vagolytic and sympathotonic states (26, 38).

One of the best ways to quantitatively analyze changes in the arterial baroreflex over an entire operating range may be analysis using a baroreflex equilibrium diagram (10, 23, 31) (see APPENDIX for details). Briefly, the baroreflex equilibrium diagram consists of a neural arc representing SNA as a function of baroreceptor input pressure and a peripheral arc representing AP as a function of SNA. The intersection of the two arcs corresponds to an operating point of the AP regulation under baroreflex closed-loop conditions. Considering the reduced AP and SNA found in previous studies, we hypothesized that short-term electroacupuncture resets the arterial baroreflex neural arc to lower SNA. In the present study, to test this hypothesis, we constructed a baroreflex equilibrium diagram with neural and peripheral arcs in anesthetized rabbits. The present findings indicate that electroacupuncture resets the baroreflex neural arc to lower SNA, moving the closed-loop operating point toward lower AP and SNA.

MATERIALS AND METHODS

Surgical Preparation

Animals were cared for in strict accordance with the *Guiding Principles for the Care and Use of Animals in the Field of Physiological Sciences* approved by the Physiological Society of Japan. Twenty-two Japanese White rabbits weighing 2.4–3.3 kg were anesthetized via intravenous injection (2 ml/kg) with a mixture of urethane (250 mg/ml) and α-chloralose (40 mg/ml) and mechanically ventilated with oxygen-enriched room air. Supplemental doses were injected as necessary (0.5 ml/kg) to maintain an appropriate level of anesthesia. Body temperature was maintained at ~38°C with a heating pad. AP was measured by using a high-fidelity pressure transducer (SPC-330A, Millar Instruments, Houston, TX) inserted via the left femoral artery. To record cardiac SNA, we exposed the left cardiac sympathetic nerve through a midline thoracotomy and attached a pair of stainless steel wire electrodes (Bioflex wire AS633, Cooner Wire, Chatsworth, CA) to the nerve. The nerve fibers peripheral to the

Address for reprint requests and other correspondence: D. Michikami, Dept. of Cardiovascular Dynamics, Advanced Medical Engineering Center, National Cardiovascular Center Research Institute, 5–7-1 Fujishirodai, Suita, Osaka 565–8565, Japan (e-mail: dmichi@ri.ncvc.go.jp or kamiya@ri.ncyc.go.jp).

The costs of publication of this article were defrayed in part by the payment of page charges. The article must therefore be hereby marked "*advertisement*" in accordance with 18 U.S.C. Section 1734 solely to indicate this fact.

electrodes were sectioned to eliminate afferent signals from the heart. To insulate and fix the electrodes, the nerves and electrodes were secured with silicone glue (Kwik-Sil, World Precision Instruments, Sarasota, FL). The preamplified nerve signals were band-pass filtered at 150–1,000 Hz, full-wave rectified, and low-pass filtered at a cutoff frequency of 30 Hz by using analog circuit. After that, the neural signals were recorded at a sampling rate of 200 Hz using a 12-bit analog-to-digital converter. Pancuronium bromide (0.1 mg/kg) was administered to prevent contaminating muscular activities. At the end of the experiment, the experimental animals were killed by an overdose of intravenous pentobarbital sodium, and the background noise level of SNA was determined postmortem.

Sixteen of the 22 rabbits were used in *protocol 1 (protocols 1-1, 1-2, and 1-3),* and the remaining 6 rabbits were used in *protocols 2, 3,* and *4*. In 10 of the 16 rabbits for *protocols 1-2* and/or *1-3* described below, we isolated both carotid sinuses from the systemic circulation by ligating the internal and external carotid arteries and other small branches originating from the carotid sinus regions. The isolated carotid sinuses were filled with warmed physiological saline through catheters inserted via the common carotid arteries. The intra-carotid sinus pressure (CSP) was controlled by a servo-controlled piston pump (model ET-126A, Labworks, Costa Mesa, CA). In the baroreflex open-loop experimental settings, bilateral vagal and aortic depressor nerves were sectioned at the neck to minimize reflex effects from cardiopulmonary regions and the aortic arch.

Electroacupuncture

Two stainless steel needles were inserted at the one-fifth point (from the knee) and the midpoint of the knee-ankle distance of approximately 30–35 mm. These needles with a diameter of 0.2 mm (CE0123, Seirin-Kasei, Shimizu City, Japan) were inserted to a depth of ~10 mm in the skin and underlying muscle (the right tibialis anterior muscle). This area corresponds to the Zusanli and Xiajuxu acupoints (over the peroneal nerve below the knee, stomach meridian, St 36 and 39) in humans.

As in previous studies (2, 3, 17, 42), the stimulus current intensity was determined as 10 times of twitch threshold, which is the minimal electrical current required for eliciting visible muscle twitches of the stimulated leg. Actually, the current was 4.8 ± 0.3 mA (4.2–5.4 mA). An electric rectangular wave current with a frequency of 1 Hz and with pulse duration of 5 ms was passed between these two needles by using an electrical stimulator (SEN-7203, Nihon Kohden) except *protocol 4* where shorter pulse durations were challenged.

Protocols

The experimental protocol was approved by the Animal Experimental Committee of National Cardiovascular Center Research Institute.

Protocol 1: effect of Zusanli electroacupuncture on AP, SNA, and baroreflex. PROTOCOL 1-1 (BAROREFLEX CLOSED-LOOP CONDITION, N = 6). To elucidate the overall cardiovascular inhibitory effects of electroacupuncture, we performed 1 Hz electroacupuncture for 8 min and measured AP and SNA responses under conditions of intact cardiovascular reflexes. In this closed-loop protocol, vagal and aortic depressor nerves were preserved. Baseline data were measured for 1 min before acupuncture insertion. At 10 min after acupuncture insertion, baseline data were measured again for 1 min. Electroacupuncture was applied for 8 min. The recovery data were measured for 2 min after the cessation of electroacupuncture.

PROTOCOL 1-2 (BAROREFLEX OPEN-LOOP CONDITION, N = 8). To elucidate the effects of electroacupuncture on the arterial baroreflex over an entire operating range, we performed a baroreflex open-loop experiment as follows. CSP was first decreased to 40 mmHg. After attainment of a steady state, CSP was increased from 40 to 160 mmHg in increments of 20 mmHg. Each pressure step was maintained for 60 s. We measured AP and SNA during the stepwise increase in CSP. Two trials (control and electroacupuncture trials) were performed on each rabbit. The order of the trials was randomized. The electroacupuncture trial was identical to the control trial except that electroacupuncture was commenced 1 min before the initiation of stepwise increase in CSP.

PROTOCOL 1-3 (BAROREFLEX OPEN-LOOP CONDITION WITH PERONEAL DENERVATION, N = 6). To identify the afferent pathway of electroacupuncture, we examined the effects of 1 Hz electroacupuncture on the arterial baroreflex after severing the right peroneal nerve at the level of the knee joint. Estimation of the baroreflex equilibrium diagram was conducted as in *protocol 1-2* in the control and electroacupuncture trials. Four of the six rabbits had also undergone *protocol 1-2*.

Protocol 2: effects of sham (nonelectrical) acupuncture at Zusanli and control (nonspecific) electrical and nonelectrical acupunctures on AP and SNA in baroreflex closed-loop condition (n = 6). To determine whether changes in AP and SNA during Zusanli electroacupuncture are specific responses, sham and control acupunctures were conducted under the following acupuncture conditions: *1*) no acupuncture (nonacupuncture), *2*) nonelectrical acupuncture at Zusanli-Xiajuxu (St 36–39) acupoints (sham acupuncture), *3*) nonelectrical acupuncture at Guangming-Xuanzhong (gallbladder meridian, Gb 37–39) acupoints (control acupuncture), and *4*) electrical acupuncture at Guangming-Xuanzhong acupoints (control electroacupuncture). We chose Guangming-Xuanzhong as nonspecific control acupoints (*trials 3* and *4*) because these acupoints are believed to reduce leg pain without affecting the cardiovascular system, in contrast to the Zusanli-Xiajuxu acupoints. In each trial, AP and SNA were measured for a baseline duration of 1 min, under acupuncture condition (*trial 1, 2, 3,* or *4*) for 8 min, and recovery for 1 min.

Protocol 3: effect of long-term Zusanli electroacupuncture on AP and SNA in baroreflex closed-loop condition (n = 6). To clarify the effect of long-term electroacupuncture on cardiovascular system, AP and SNA were measured during and after 30 min of electroacupuncture at Zusanli-Xiajuxu acupoints. *Protocol 3* was conducted in the same manner as *protocol 1-1* except with a longer stimulation duration than *protocol 1-1* (8 min).

Protocol 4: Effect of pulse duration of Zusanli electroacupuncture on AP and SNA in baroreflex closed-loop condition (n = 6). To examine the effect of pulse duration of electroacupuncture on AP and SNA, AP and SNA were measured during electroacupuncture at Zusanli-Xiajuxu acupoints with the pulse duration increasing stepwise from 0.1 to 0.25, 0.5, 1, 2.5, 5, and 10 ms, every 60 s. In each animal, the frequency and stimulus current intensity were maintained constant as in *protocols 1, 2,* and *3*.

Data Analysis

We recorded CSP, SNA, and AP at a sampling rate of 200 Hz by using a 12-bit analog-to-digital converter. Data were stored on the hard drive of a dedicated laboratory computer system for later analyses.

In *protocol 1-1, 2, and 4*, mean AP and SNA for 1 min were calculated for baseline conditions, every minute of electroacupuncture, and recovery. In *protocol 3*, mean AP and SNA for 5 min were calculated for baseline conditions, electroacupuncture, and recovery. In *protocols 1-2* and *1-3*, we calculated mean AP and SNA during the last 10 s of each CSP step. Because the absolute magnitude of SNA depended on recording conditions, SNA was presented in arbitrary units (au). The background noise level was set at 0 au and the SNA value at the closed-loop operating point in the control trial (without electroacupuncture) was set at 100 au for each animal.

A four-parameter logistic function analysis was performed on the neural arc (CSP-SNA data pairs) and the peripheral arc (SNA-AP data pairs) as follows (11)